

Detection of Gamma Ray Emission from the Sagittarius Dwarf Spheroidal Galaxy

Roland Crocker (✉ rcrocker@fastmail.fm)

Australian National University <https://orcid.org/0000-0002-2036-2426>

Oscar Macias

University of Amsterdam <https://orcid.org/0000-0001-8867-2693>

Dougal Mackey

Australian National University <https://orcid.org/0000-0002-6529-8093>

Mark Krumholz

Australian National University

Shin'ichiro Ando

University of Amsterdam

Shunsaku Horiuchi

Virginia Tech <https://orcid.org/0000-0001-6142-6556>

Matthew Baring

Rice University <https://orcid.org/0000-0003-4433-1365>

Chris Gordon

University of Canterbury <https://orcid.org/0000-0003-4864-5150>

Thomas Venville

Swinburne University of Technology

Alan Duffy

Swinburne University of Technology <https://orcid.org/0000-0002-9636-1809>

Rui-Zhi Yang

University of Science and Technology of China

Felix Aharonian

Max-Planck-Institut für Kernphysik <https://orcid.org/0000-0003-1157-3915>

James Hinton

Max-Planck Institute for Nuclear Physics

Deheng Song

Virginia Tech

Ashley Ruiter

University of New South Wales Canberra <https://orcid.org/0000-0002-4794-6835>

Miroslav Filipovic

Western Sydney University <https://orcid.org/0000-0002-4990-9288>

Physical Sciences - Article

Keywords: Fermi Bubbles, gamma ray emission, Sagittarius dwarf spheroidal galaxy

Posted Date: October 28th, 2021

DOI: <https://doi.org/10.21203/rs.3.rs-1025965/v1>

License:  This work is licensed under a Creative Commons Attribution 4.0 International License.

[Read Full License](#)

Detection of Gamma-Ray Emission from the Sagittarius Dwarf Spheroidal Galaxy

Roland M. Crocker^{1,10,*+,}, Oscar Macias^{2,3,†,+}, Dougal Mackey¹, Mark R. Krumholz¹, Shin'ichiro Ando^{2,3}, Shunsaku Horiuchi^{4,3}, Matthew G. Baring⁵, Chris Gordon⁶, Thomas Venville⁷, Alan R. Duffy⁷, Rui-Zhi Yang^{8,9,10}, Felix Aharonian^{10,11}, J. A. Hinton¹⁰, Deheng Song⁴, Ashley J. Ruiter¹², and Miroslav D. Filipović¹³

¹Research School of Astronomy and Astrophysics, Australian National University, Canberra 2611, A.C.T., Australia

²GRAPPA – Gravitational and Astroparticle Physics Amsterdam, University of Amsterdam, Science Park 904, 1098

⁹XH Amsterdam, The Netherlands

¹⁰Kavli IPMU (WPI), UTIAS, The University of Tokyo, Kashiwa, Chiba 277-8583, Japan

¹¹Center for Neutrino Physics, Department of Physics, Virginia Tech, Blacksburg, Virginia 24061, USA

¹²Department of Physics and Astronomy - MS 108, Rice University, 6100 Main Street, Houston, Texas 77251-1892,
¹³USA

¹⁴School of Physical and Chemical Sciences, University of Canterbury, Christchurch, New Zealand

¹⁵Centre for Astrophysics and Supercomputing, Swinburne University of Technology, PO Box 218, Hawthorn, VIC
¹⁶3122, Australia

¹⁷Department of Astronomy, School of Physical Sciences, University of Science and Technology of China, Hefei,
¹⁸Anhui 230026, China

¹⁹CAS Key Laboratory for Research in Galaxies and Cosmology, University of Science and Technology of China,
²⁰Hefei, Anhui 230026, China

²¹School of Astronomy and Space Science, University of Science and Technology of China, Hefei, Anhui 230026,
²²China

²³Max-Planck-Institut für Kernphysik, Saupfercheckweg 1, 69117 Heidelberg, Germany

¹¹Dublin Institute for Advanced Studies, 31 Fitzwilliam Place, Dublin 2, Ireland

²⁵School of Science, University of New South Wales Canberra, The Australian Defence Force Academy, 2600 ACT,
²⁶Canberra, Australia

¹³Western Sydney University, Locked Bag 1797, Penrith South DC, NSW 2751, Australia

²⁸*rcrocker@fastmail.fm

²⁹†o.a.maciasramirez@uva.nl

³⁰⁺These authors contributed equally to this work.

31 **ABSTRACT**

The Fermi Bubbles are giant, γ -ray emitting lobes emanating from the nucleus of the Milky Way[1, 2] discovered in \sim 1-100 GeV data collected by the Large Area Telescope on board the *Fermi* Gamma-Ray Space Telescope[3]. Previous work[4] has revealed substructure within the Fermi Bubbles that has been interpreted as a signature of collimated outflows from the Galaxy's super-massive black hole. Here we show that much of the γ -ray emission associated to the brightest region of substructure – the so-called *cocoon* – is actually due to the Sagittarius dwarf spheroidal (Sgr dSph) galaxy. This large Milky Way satellite is viewed through the Fermi Bubbles from the position of the Solar System. As a tidally and ram-pressure stripped remnant, the Sgr dSph has no on-going star formation, but we demonstrate that its γ -ray signal is naturally explained by inverse Compton scattering of cosmic microwave background photons by high-energy electron-positron pairs injected by the dwarf's millisecond pulsar (MSP) population, combined with these objects' magnetospheric emission. This finding suggests that MSPs likely produce significant γ -ray emission amongst old stellar populations, potentially confounding indirect dark matter searches in regions such as the Galactic Centre, the Andromeda galaxy, and other massive Milky Way dwarf spheroidals.

33 Early analysis of data from the *Fermi* Large Area Telescope (*Fermi*-LAT) identified two counter-propagating, co-linear γ -ray
34 substructures within the Fermi Bubbles (FBs; Figure 1a), a *jet* in the northern Galactic hemisphere and *cocoon* in the south[4];
35 subsequent, independent analyses[2, 5] have only confirmed the existence of the latter. Since the cocoon is contained within the
36 solid angle of the surrounding FBs and exhibits a similar γ -ray spectrum, it is natural to propose they share a common origin.
37 However, the cocoon is also spatially coincident with the Sagittarius dwarf spheroidal galaxy (Sgr dSph [6]; Figure 1b). The
38 chance probability of such an alignment is low, $\sim 1\%$ (see the Supplementary Information; S.I.), even before accounting for
39 the fact that the cocoon and the Sgr dSph have similar shapes and orientations. Moreover, at a distance of only 26.5 kpc [7],
40 Sgr dSph is one of the closest and, at $\sim 10^8 M_\odot$, [8] (where M_\odot denotes the solar mass), most massive galactic satellites of the
41 Milky Way (MW). Indeed, the Sgr dSph has the largest mass divided by distance squared of *any* astronomical object not yet
42 detected in γ -rays.

43 We therefore consider emission from the Sgr dSph as an alternative origin for the cocoon. In order to test this possibility, we
44 fit the γ -ray emission observed by *Fermi*-LAT over a region of interest (ROI) containing the cocoon via template analysis. In our
45 *baseline* model these templates include only known point sources and sources of Galactic diffuse γ -ray emission. We contrast
46 the baseline with a *baseline + Sgr dSph* model that invokes these same templates plus an additional template constructed to be
47 spatially coincident with the bright stars of the Sgr dSph; full details of the fitting procedure are provided in Methods and S.I.
48 Using the best motivated choice of templates, we find that the baseline + Sgr dSph model is preferred at 8.1σ significance over
49 the baseline model. We also repeat the analysis for a wide range of alternative templates for both Galactic diffuse emission and
50 for the Sgr dSph (Table 1 and Extended Data (E.D.) Figure 4); the only template combination for which the detection of γ -rays
51 from the Sgr dSph drops below 5σ is one using a sparse template of < 1000 stars for the Sgr dSph. Moreover, even this is an
52 extremely conservative estimate, because our baseline model uses a structured template for the FBs that absorbs some of the

53 signal that is spatially coincident with the Sgr dSph into a structure of unknown origin. If we follow the method recommended
54 by the Fermi collaboration [2] and use a flat FB template in our analysis, the significance of our detection of the Sgr dSph is
55 always $> 14\sigma$. Despite this, for the remainder of our analysis we follow the most conservative choice by using the structured
56 template in our baseline model.

57 These results provide strong statistical evidence for a signal coming from the Sgr dSph, but nevertheless we also carry out a
58 series of additional tests to check its robustness, which we discuss in Methods. Specifically, we verify that (1) the residuals
59 between our best-fitting model and the data are consistent with photon counting statistics (E.D. [Figure 5](#) and [Figure 6](#)), (2) our
60 pipeline reliably recovers signals comparable to that of the observed Sgr dSph from synthetic data where we artificially inject
61 such a signal (E.D. [Figure 7](#)), and (3) if we allow the Sgr dSph template to be rotated arbitrarily on the sky, the best-fitting
62 position angle is very close to the actual one (E.D. [Figure 8](#)). We have also tried the experiment of displacing the Sgr dSph stellar
63 template from its observed position in the γ -ray analysis. From this we find moderate (4.5σ significance) evidence that the
64 best-fitting position is slightly displaced from the observed position of the Sgr dSph by approximately 4 degrees. Given this
65 apparent displacement is in a direction very closely aligned with the dwarf galaxy's direction of travel (E.D. [Figure 8](#)) it it
66 plausibly represents a small, but real and expected (as explained below) physical offset between the stars and the γ -ray emission.

67 The directly-measured flux from the Sgr dSph, derived from our fiducial choice of templates, corresponds to a luminosity
68 of $(3.8 \pm 0.6) \times 10^{36}$ erg/s (1σ error) for γ -ray photons in the range from 0.5 to 150 GeV (equivalently $\sim 4 \times 10^{28}$ erg/s/ M_\odot).
69 Over this range the spectrum is approximately described by a hard power law $dF_\gamma/dE_\gamma \propto E_\gamma^{-2.1}$ ([Figure 2](#)); on the basis of the
70 lowest energy datum, there is marginal evidence for spectral hardening below \sim GeV. There is no evidence for a cut-off at high
71 energies. We show in E.D. [Figure 9](#) that this spectral shape is qualitatively insensitive to the choice of foreground templates,
72 and E.D. [Figure 10](#) demonstrates that the spectra we recover for the various foregrounds within the ROI remain physically
73 plausible when we introduce a Sgr dSph template.

74 Since our template fits strongly suggest that there is a real γ -ray emission component tracing the Sgr dSph, a natural next
75 question is what mechanism could be responsible for producing it. The core of the Sgr dSph is the remnant of a once much
76 more massive galaxy that has suffered severe tidal disruption by the MW's gravitational field; leading and trailing streams of
77 stars from this progenitor wrap around the sky[9]. Tidal and ram pressure stripping, moreover, have robbed the Sgr dSph of the
78 gas required to fuel the formation of new stars; consequently, no star formation has recently occurred in the dwarf. However, it
79 did experience punctuated bursts of star formation [10] – triggered by its crossings through the Galactic plane [11] – up to
80 the time when it lost all its gas. In the MW, the dominant source of diffuse γ -ray emission is collisions between (hadronic)
81 cosmic rays (CRs) and ambient interstellar medium (ISM) gas nuclei[12]. Such diffuse hadronic γ -ray emission is ruled out for
82 the Sgr dSph because of the lack of dense ‘target’ gas. Besides, the Milky Way's hadronic CRs are dominantly accelerated
83 at astrophysical shocks produced by short-lived massive stars and their supernova explosions, which cease ~ 40 Myr after
84 star formation. In comparison, $\sim 2 - 3$ Gyr [13] have elapsed since the Sgr dSph last formed significant numbers of stars.
85 Stellar γ -ray emission is also ruled out as an explanation of the Sgr dSph signal: while our Sun is a source of ~ 100 GeV

86 γ -rays, this emission is again dominantly due to collisions between hadronic CRs from the wider Galaxy and Solar gas; γ -ray
87 emission from non-thermal particles accelerated by the Sun itself only extends to 4 GeV [14]. This leaves two possibilities for
88 the Sgr dSph γ -ray signal: it is created from the self-annihilation of dark matter (DM) particles in the dwarf's DM halo, or by
89 millisecond pulsars (MSPs) deriving from the stars of the Sgr dSph.

90 Although tantalizing, it is also unlikely that the Sgr dSph γ -ray signal is due to DM. This follows from the very fact that
91 the signal largely traces the stars of the dwarf, while N-body simulations [11] show that the Milky Way's tidal field will have
92 overwhelmingly dispersed the progenitor galaxy's original DM halo into the stream over its orbital history. On the other
93 hand, the spatial correspondence is elegantly explained if the γ -rays ultimately emerge from a stellar source that, non-trivially,
94 shares the same projected spatial distribution as the general population of the Sgr dSph stars; the MSP scenario can naturally
95 accommodate this.

96 An MSP origin of the Sgr dSph signal is plausible given MSPs' long spin-down timescale, $\gtrsim \mathcal{O}(\text{Gyr})$, the fact that they
97 radiate some part of their magnetic dipole luminosity into γ -rays, and that they share approximately the same projected spatial
98 distribution as the other stars in the dwarf. However, there are two significant challenges to this scenario: First, the inferred
99 γ -ray luminosity per unit stellar mass is much larger ($\gtrsim 10\times$) for the Sgr dSph than for some other systems whose detected
100 γ -ray emission is plausibly dominated by MSPs including the Galactic Bulge [15–19] and Andromeda[20, 21] (M31), the giant
101 spiral galaxy nearest to the Milky Way (cf. Figure 3). Second, the hard, $\approx E_\gamma^{-2.1}$ spectrum of the Sgr dSph (Figure 2) does not
102 resemble the classic \sim few GeV bump (in the spectral energy distribution) of the magnetospheric γ -ray signal detected from
103 MSPs (or the globular clusters (GCs) that are known to host them: e.g. [22]).

104 However, both of these challenges can be overcome by considering how the differences between the Sgr dSph environment
105 and other MSP-hosting systems will affect the γ -ray signal. First, note that while the spectrum of the Sgr dSph does not
106 resemble an MSP magnetospheric signal, it does resemble inverse Compton (IC) emission from the up-scattering (by a CR
107 electron-positron population; e^\pm) of ambient light which, for the Sgr dSph, is dominated by the Cosmic Microwave Background
108 (CMB). We also know that MSPs produce e^\pm with energies of at least a few TeV, since these are the particles that ultimately
109 drive the observed GeV MSP γ -ray photospheric emission. Some of these e^\pm will give up all their energy within the MSP
110 magnetosphere. However, given the expected absence of wind nebulae or supernova remnants surrounding these old, low
111 luminosity objects [23], many will freely escape both magnetosphere and MSP environs into the larger Sgr dSph environment
112 [24, 25]. Here the e^\pm will scatter CMB photons and produce an IC signal exactly like the one that we have detected. In an
113 environment like Andromeda or the Galactic Bulge, this IC signal will be weak (albeit detectable in the case of the Bulge
114 according to [19]), because much of the escaping e^\pm energy will be lost to synchrotron rather than IC radiation. In an ultra-gas
115 poor system like the Sgr dSph, however, we expect the ISM magnetic field to be far weaker than in a gas-rich galaxy[26] with
116 an energy density significantly smaller than that in the CMB; thus radiative losses from MSP-escaping e^\pm are overwhelmingly
117 into IC rather than synchrotron radiation. This yields, per stellar mass, far more γ -ray emission (and far less emission at
118 other energies) than is produced by MSPs in more gas-rich environments and explains the dwarf's very hard γ -ray spectrum.

119 Consistent with this explanation, globular clusters – which are also gas-poor and weakly-magnetized – represent another
120 environment where MSP-driven γ -ray emission seems to sometimes include a significant IC component[22]. We formalize this
121 intuitive argument in Methods, where we show that the spectrum of the Sgr dSph is extremely well fit as a combination of IC
122 and magnetospheric radiation with self-consistently related spectral parameters.

123 A putative IC contribution would also naturally explain why we obtain a better fit for a template displaced to Galactic
124 south-west of its true position by $\sim 4^\circ$, or about 1.9 kpc (E.D. [Figure 8](#), right) than for one coincident with the true position
125 of the dwarf. The Northward proper motion of the Sgr dSph [27] means this displacement is backwards along its path. As
126 the Sgr dSph plunges through the Milky Way halo, the magnetic field around it will be elongated into a magnetotail oriented
127 backwards along its trajectory, and e^\pm emitted into the dwarf will be trapped by these magnetic field lines, leading them to
128 accumulate and emit in a position that trails the Sgr dSph, exactly as we observe. We offer a more quantitative evaluation of
129 this scenario in the S.I.

130 We finally remark on two other effects that may contribute to the marked γ -ray brightness of the Sgr dSph. First, the
131 dwarf has a much lower metallicity than the Milky Way disc or bulge, or M31, and the incidence of MSPs is expected to be
132 appreciably higher in metal-poor systems than in metal-rich ones [28]. Second, as a fraction of the overall population, the
133 Sgr dSph contains many more relatively young stars than either M31 or the Galactic bulge, and MSPs associated with such \sim
134 few Gyr old stars will be significantly γ -ray brighter [19] than those associated to the dominant 8-12 Gyr old stellar populations
135 of the bulge or M31. Indeed, our best-fit total luminosity for the Sgr dSph is entirely consistent with the predictions of recent
136 binary population synthesis modelling [19] for the spin-down luminosity of MSP populations at ages comparable to the last
137 episode of star formation in the Sgr dSph.

138 There are a number of implications of the discovery of γ -rays from the Sgr dSph. Firstly, this study largely removes
139 any residual motivation for the idea that Fermi Bubbles sub-structure be interpreted as γ -ray jets launched from the Galactic
140 nucleus. Secondly, in the context of searches for the signatures of DM annihilation, it unfortunately appears that astrophysical
141 backgrounds in dwarf spheroidal galaxies can be stronger than previously appreciated. Thirdly, our results motivate the
142 introduction of stellar templates into the analysis of data from all γ -ray resolved galaxies (M31, Large and Small Magellanic
143 Clouds) to probe the contribution of MSPs. In general, our study lends support to the argument [23] that MSPs contribute
144 significantly to the energy budget of CR e^\pm in galaxies with low specific star-formation rates.

145 Supplementary Information is available for this paper. Correspondence and requests for materials should be addressed to
146 RMC or OM. Reprints and permissions information is available at www.nature.com/reprints.

147 **References**

- 148 1. Su, M., Slatyer, T. R. & Finkbeiner, D. P. Giant Gamma-ray Bubbles from Fermi-LAT: Active Galactic Nucleus Activity
149 or Bipolar Galactic Wind? *Astrophys. J.* **724**, 1044–1082. doi:[10.1088/0004-637X/724/2/1044](https://doi.org/10.1088/0004-637X/724/2/1044) (2010).
- 150 2. Ackermann, M. et al. The Spectrum and Morphology of the Fermi Bubbles. *Astrophys. J.* **793**, 64. doi:[10.1088/0004-637X/793/1/64](https://doi.org/10.1088/0004-637X/793/1/64) (2014).
- 151 3. Atwood, W. B. et al. The Large Area Telescope on the Fermi Gamma-Ray Space Telescope Mission. *Astrophys. J.* **697**,
152 1071–1102. doi:[10.1088/0004-637X/697/2/1071](https://doi.org/10.1088/0004-637X/697/2/1071) (2009).
- 153 4. Su, M. & Finkbeiner, D. P. Evidence for Gamma-Ray Jets in the Milky Way. *Astrophys. J.* **753**, 61. doi:[10.1088/0004-637X/753/1/61](https://doi.org/10.1088/0004-637X/753/1/61) (2012).
- 154 5. Selig, M., Vacca, V., Oppermann, N. & Enßlin, T. A. The denoised, deconvolved, and decomposed Fermi γ -ray sky. An
155 application of the D³PO algorithm. *Astron. Astrophys.* **581**, A126. doi:[10.1051/0004-6361/201425172](https://doi.org/10.1051/0004-6361/201425172) (2015).
- 156 6. Ibata, R. A., Gilmore, G. & Irwin, M. J. A dwarf satellite galaxy in Sagittarius. *Nature* **370**, 194–196. doi:[10.1038/370194a0](https://doi.org/10.1038/370194a0) (1994).
- 157 7. Vasiliev, E. & Belokurov, V. The last breath of the Sagittarius dSph. *Mon. Not. R. Astron. Soc.* **497**, 4162–4182.
158 doi:[10.1093/mnras/staa2114](https://doi.org/10.1093/mnras/staa2114) (2020).
- 159 8. Vasiliev, E., Belokurov, V. & Erkal, D. Tango for three: Sagittarius, LMC, and the Milky Way. *Mon. Not. R. Astron. Soc.*
160 **501**, 2279–2304. doi:[10.1093/mnras/staa3673](https://doi.org/10.1093/mnras/staa3673) (2021).
- 161 9. Belokurov, V. et al. The Field of Streams: Sagittarius and Its Siblings. *Astrophys. J. Lett.* **642**, L137–L140. doi:[10.1086/504797](https://doi.org/10.1086/504797) (2006).
- 162 10. Weisz, D. R. et al. The Star Formation Histories of Local Group Dwarf Galaxies. I. Hubble Space Telescope/Wide Field
163 Planetary Camera 2 Observations. *Astrophys. J.* **789**, 147. doi:[10.1088/0004-637X/789/2/147](https://doi.org/10.1088/0004-637X/789/2/147) (2014).
- 164 11. Tepper-García, T. & Bland-Hawthorn, J. The Sagittarius dwarf galaxy: where did all the gas go? *Mon. Not. R. Astron. Soc.*
165 **478**, 5263–5277. doi:[10.1093/mnras/sty1359](https://doi.org/10.1093/mnras/sty1359) (2018).
- 166 12. Strong, A. W. et al. Global Cosmic-ray-related Luminosity and Energy Budget of the Milky Way. *Astrophys. J. Lett.* **722**,
167 L58–L63. doi:[10.1088/2041-8205/722/1/L58](https://doi.org/10.1088/2041-8205/722/1/L58) (2010).
- 168 13. Siegel, M. H. et al. The ACS Survey of Galactic Globular Clusters: M54 and Young Populations in the Sagittarius Dwarf
169 Spheroidal Galaxy. *Astrophys. J. Lett.* **667**, L57–L60. doi:[10.1086/522003](https://doi.org/10.1086/522003) (2007).
- 170 14. Linden, T. et al. Evidence for a New Component of High-Energy Solar Gamma-Ray Production. *Phys. Rev. Lett.* **121**,
171 131103. doi:[10.1103/PhysRevLett.121.131103](https://doi.org/10.1103/PhysRevLett.121.131103) (2018).

- 176 15. Abazajian, K. N. The consistency of Fermi-LAT observations of the galactic center with a millisecond pulsar population
177 in the central stellar cluster. *J. Cosmology Astropart. Phys.* **2011**, 010. doi:[10.1088/1475-7516/2011/03/010](https://doi.org/10.1088/1475-7516/2011/03/010)
178 (2011).
- 179 16. Macias, O. et al. Galactic bulge preferred over dark matter for the Galactic centre gamma-ray excess. *Nature Astronomy* **2**,
180 387–392. doi:[10.1038/s41550-018-0414-3](https://doi.org/10.1038/s41550-018-0414-3) (2018).
- 181 17. Bartels, R., Storm, E., Weniger, C. & Calore, F. The Fermi-LAT GeV excess as a tracer of stellar mass in the Galactic
182 bulge. *Nature Astronomy* **2**, 819–828. doi:[10.1038/s41550-018-0531-z](https://doi.org/10.1038/s41550-018-0531-z) (2018).
- 183 18. Macias, O. et al. Strong evidence that the galactic bulge is shining in gamma rays. *J. Cosmology Astropart. Phys.* **2019**,
184 042. doi:[10.1088/1475-7516/2019/09/042](https://doi.org/10.1088/1475-7516/2019/09/042) (2019).
- 185 19. Gautam, A. et al. Millisecond Pulsars from Accretion Induced Collapse naturally explain the Galactic Center Gamma-ray
186 Excess. *arXiv e-prints*, arXiv:2106.00222 (2021).
- 187 20. Ackermann, M. et al. Observations of M31 and M33 with the Fermi Large Area Telescope: A Galactic Center Excess in
188 Andromeda? *Astrophys. J.* **836**, 208. doi:[10.3847/1538-4357/aa5c3d](https://doi.org/10.3847/1538-4357/aa5c3d) (2017).
- 189 21. Eckner, C. et al. Millisecond Pulsar Origin of the Galactic Center Excess and Extended Gamma-Ray Emission from
190 Andromeda: A Closer Look. *Astrophys. J.* **862**, 79. doi:[10.3847/1538-4357/aac029](https://doi.org/10.3847/1538-4357/aac029) (2018).
- 191 22. Song, D., Macias, O., Horiuchi, S., Crocker, R. M. & Nataf, D. M. Evidence for inverse Compton emission from globular
192 clusters. *arXiv e-prints*, arXiv:2102.00061 (2021).
- 193 23. Sudoh, T., Linden, T. & Beacom, J. F. Millisecond pulsars modify the radio-star-formation-rate correlation in quiescent
194 galaxies. *Phys. Rev. D* **103**, 083017. doi:[10.1103/PhysRevD.103.083017](https://doi.org/10.1103/PhysRevD.103.083017) (2021).
- 195 24. Baring, M. G. *Perspectives on Gamma-Ray Pulsar Emission* in *AstroPhysics of Neutron Stars 2010: A Conference in
196 Honor of M. Ali Alpar* (eds Göğüş, E., Belloni, T. & Ertan, Ü.) **1379** (2011), 74–81. doi:[10.1063/1.3629488](https://doi.org/10.1063/1.3629488).
- 197 25. Venter, C., Kopp, A., Harding, A. K., Gonthier, P. L. & Büsching, I. Cosmic-ray Positrons from Millisecond Pulsars.
198 *Astrophys. J.* **807**, 130. doi:[10.1088/0004-637X/807/2/130](https://doi.org/10.1088/0004-637X/807/2/130) (2015).
- 199 26. Regis, M. et al. Local Group dSph radio survey with ATCA - II. Non-thermal diffuse emission. *Mon. Not. R. Astron. Soc.*
200 **448**, 3747–3765. doi:[10.1093/mnras/stv127](https://doi.org/10.1093/mnras/stv127) (2015).
- 201 27. del Pino, A. et al. Revealing the Structure and Internal Rotation of the Sagittarius Dwarf Spheroidal Galaxy with Gaia and
202 Machine Learning. *Astrophys. J.* **908**, 244. doi:[10.3847/1538-4357/abd5bf](https://doi.org/10.3847/1538-4357/abd5bf) (2021).
- 203 28. Ruiter, A. J. et al. On the formation of neutron stars via accretion-induced collapse in binaries. *Monthly Notices of the
204 Royal Astronomical Society* **484**, 698–711. doi:[10.1093/mnras/stz001](https://doi.org/10.1093/mnras/stz001) (2019).

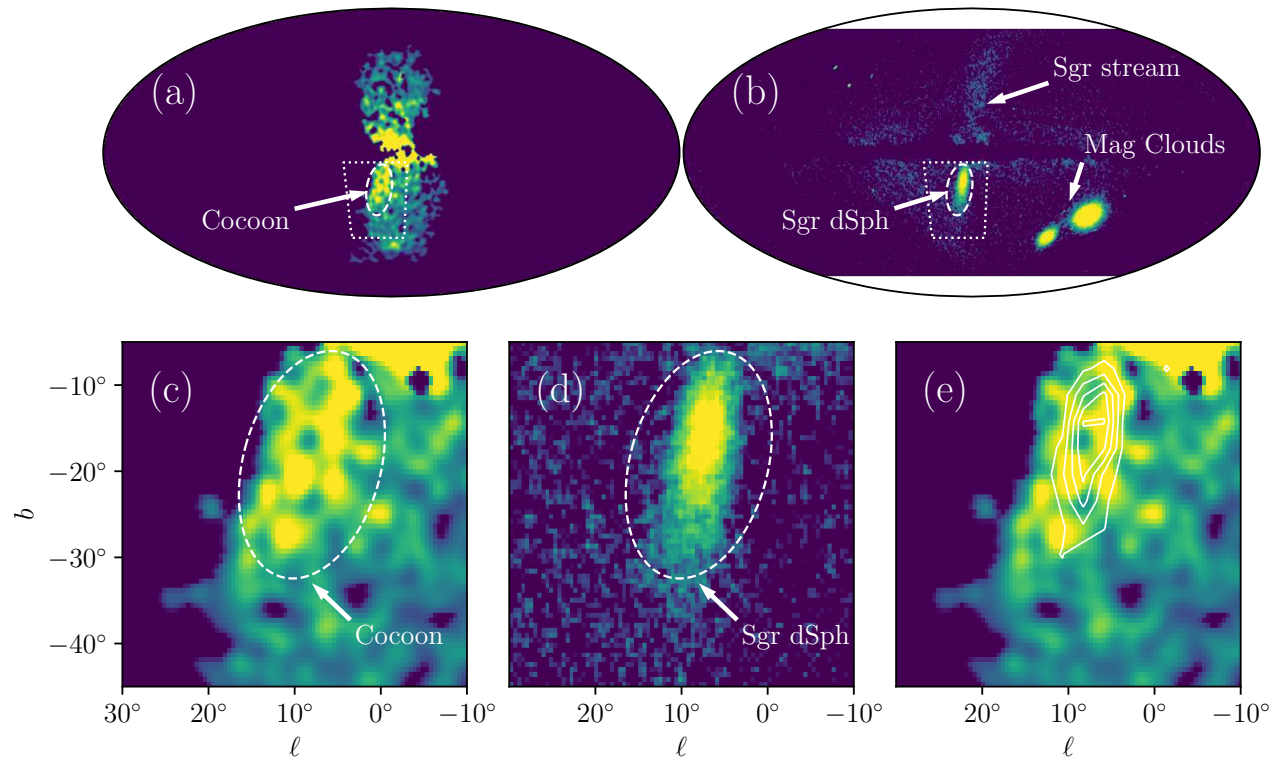


Figure 1. Panels (a) and (b) are all-sky views in Mollweide projection in Galactic coordinates of longitude ℓ and latitude b with east to the left, with the ROI marked by the dotted box. Panels (c)–(e) are in a cylindrical projection and zoom in on the ROI. **Panels (a) and (c)** display the γ -ray spatial template for the Fermi Bubbles[2] in arbitrary units with linear colour scale, highlighting the cocoon. **Panels (b) and (d)** show the angular density of RR Lyrae stars with line-of-sight distances > 20 kpc from the *Gaia* Data Release 2 (DR2), in arbitrary units with logarithmic scaling; the Sgr dSph, Sgr stream, and the Large and Small Magellanic Clouds are clearly visible. The proper motion of the Sgr dSph is upwards in this figure. The dashed ellipses in panels (a)–(d) mark the same coordinates in each panel, and highlight both the cocoon and the Sgr dSph. **Panel (e)** shows contours of RR Lyrae surface density overlaid on the Fermi Bubbles template shown as the coloured background.

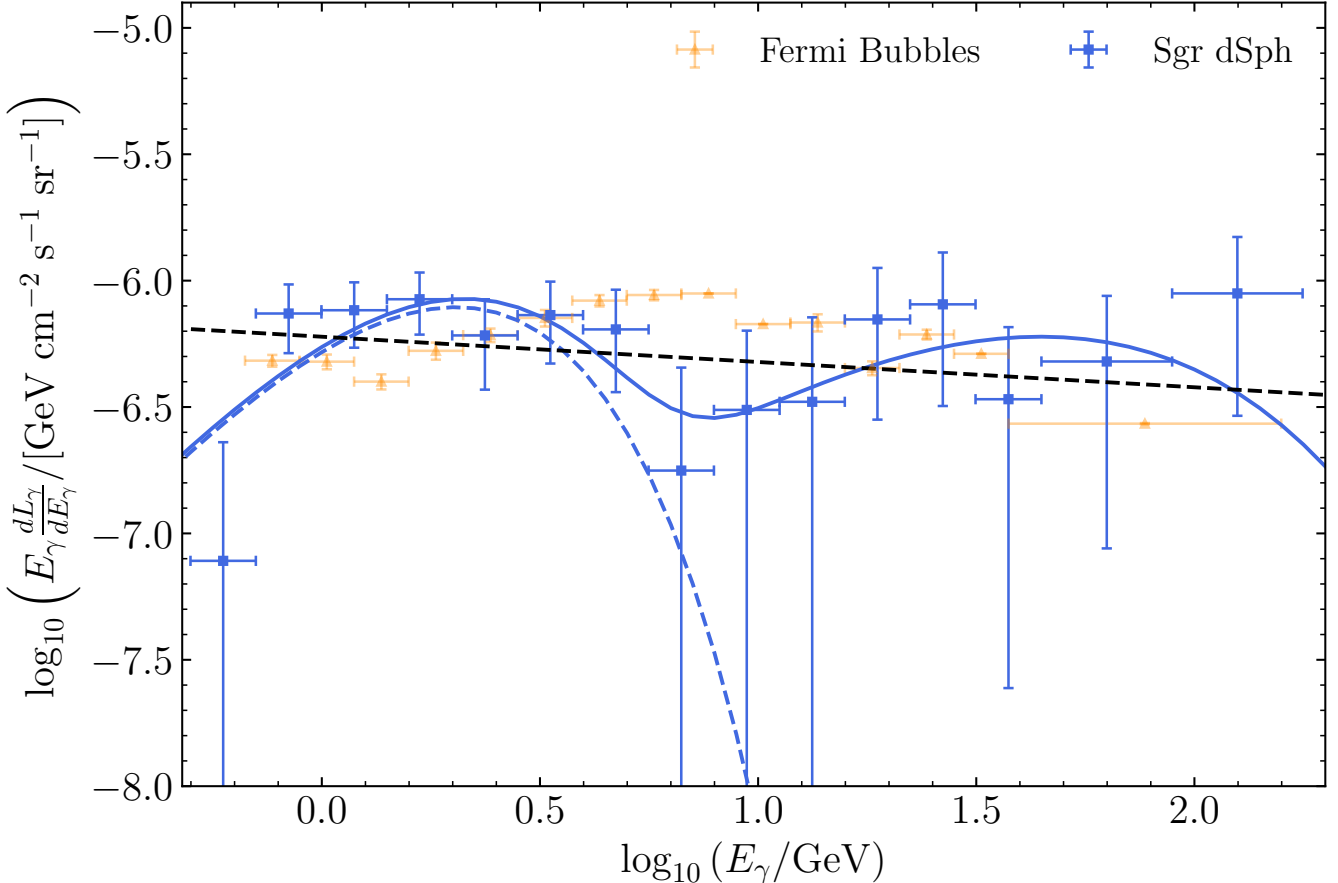


Figure 2. Measured γ -ray spectral brightness distributions of the Sgr dSph and the surrounding Fermi Bubbles; the black, dashed line shows a differential number flux obeying $dN_\gamma/dE_\gamma \propto E_\gamma^{-2.1}$. These data are as obtained by us in our *Fermi*-LAT data analysis as described in Methods. We have converted luminosities to surface brightnesses adopting source solid angles of $\Omega_{\text{Sgr dSph}} = 9.6 \times 10^{-3} \text{ sr}$, and $\Omega_{\text{FB}} = 0.49 \text{ sr}$, with the latter set by the $40^\circ \times 40^\circ$ region of interest (ROI), not the intrinsic sizes of the Bubbles (which are larger than the ROI). Error bars show 1σ errors; for the Sgr dSph, the error bars incorporate both statistical and systematic errors added in quadrature. The smooth blue curves show (solid) the best fit combined (magnetospheric + IC) and (dashed) the best fit magnetospheric spectra.

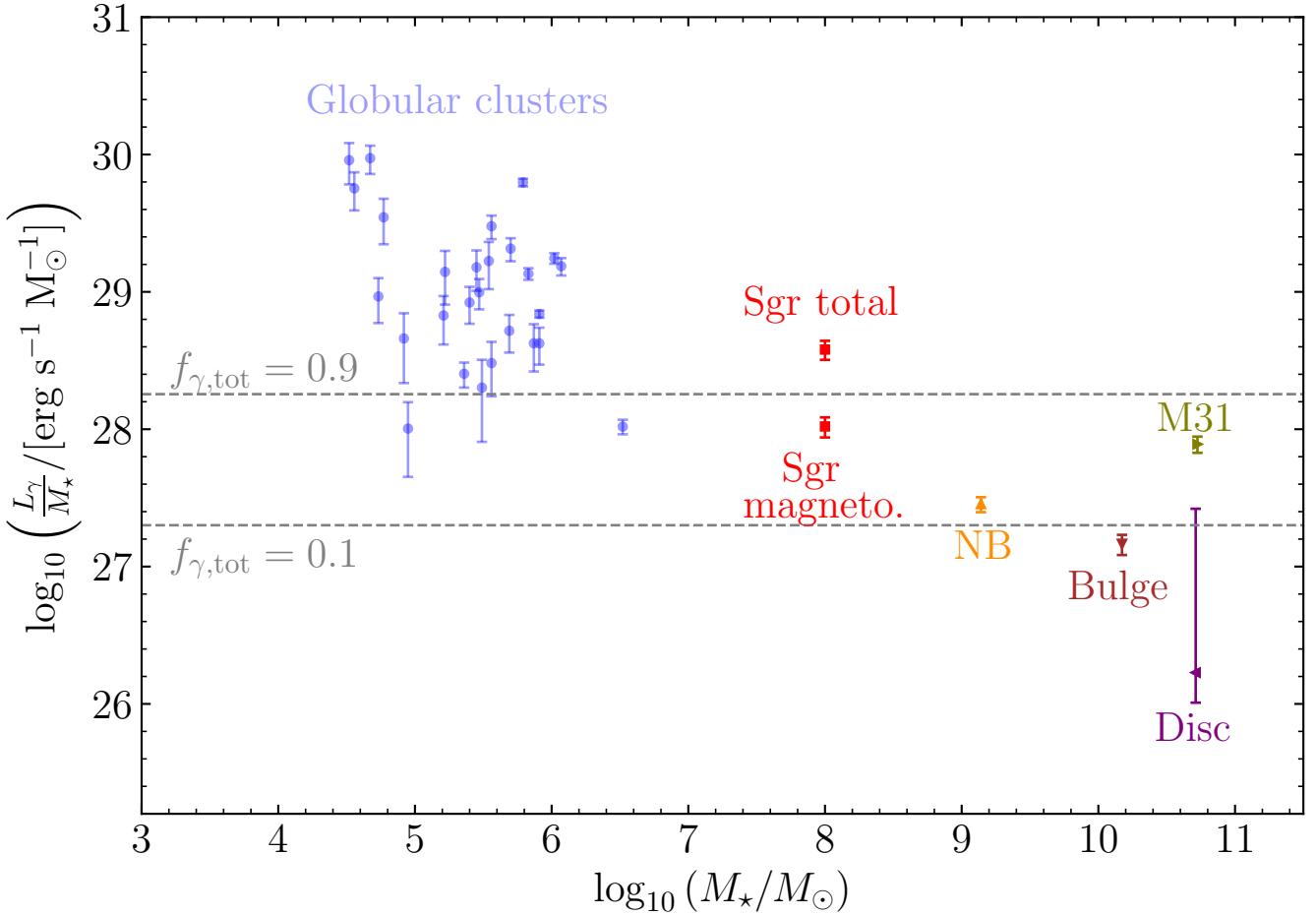


Figure 3. γ -ray luminosity normalised to stellar mass for various structures whose emission is plausibly dominated by MSPs. The ‘Sgr magneto.’ datum shows our best-fit magnetospheric luminosity per stellar mass (the spectrum shown as the dashed blue curve in Figure 2) while the ‘Sgr tot’ datum is the total, directly-measured luminosity. Globular cluster (‘GC’) measurements are from ref. [22], while the remaining data (collated by ref. [22]) are from ref. [18] (nuclear bulge of the Milky Way, ‘NB’), ref. [20] (M31), and ref. [17] (Milky Way disc). The horizontal, dashed, grey curves show the predicted total γ -ray luminosity per unit stellar mass at the nominated efficiencies, $f_{\gamma,\text{tot}} = \{0.1, 0.9\}$, given an MSP spin-down power per unit stellar mass of 2×10^{28} erg/s/ M_{\odot} as we infer from ref. [23].

Hadr. / Bremss.	Template choices				Results			
	IC	FB	Sgr dSph		$-\log(\mathcal{L}_{\text{Base}})$	$-\log(\mathcal{L}_{\text{Base+Sgr}})$	TS _{Source}	Significance
Default model								
HD	3D	S	Model I		866680.6	866633.0	95.2	8.1σ
Alternative background templates								
HD	2D A	S	Model I		866847.1	866810.9	72.3	6.9σ
HD	2D B	S	Model I		867234.9	867192.1	85.8	7.8σ
HD	2D C	S	Model I		866909.4	866868.5	81.7	7.4σ
Interpolated	3D	S	Model I		867595.4	867567.4	56.0	5.8σ
GALPROP	3D	S	Model I		866690.5	866640.8	99.5	8.3σ
Flat FB template								
HD	3D	U	Model I		867271.7	867060.1	423.2	19.1σ
HD	2D A	U	Model I		867284.2	867122.9	322.5	16.5σ
HD	2D B	U	Model I		867624.3	867464.0	320.7	16.4σ
HD	2D C	U	Model I		867322.7	867158.2	329.0	16.6σ
Interpolated	3D	U	Model I		867287.4	867081.2	412.4	18.9σ
GALPROP	3D	U	Model I		868214.6	868040.9	347.6	17.2σ
Alternative Sgr dSph templates								
HD	3D	S	Model II		866680.6	866626.3	108.5	8.7σ
HD	3D	S	Model III		866680.6	866647.5	66.1	6.4σ
HD	3D	S	Model IV		866680.6	866678.2	4.8	0.4σ
HD	3D	S	Model V		866680.6	866644.9	71.5	6.7σ
HD	3D	U	Model II		867271.7	866970.7	602.1	23.2σ
HD	3D	U	Model III		867271.7	866994.1	555.3	22.2σ
HD	3D	U	Model IV		867271.7	867152.2	239.1	14.0σ
HD	3D	U	Model V		867271.7	866993.3	556.9	22.2σ

Table 1. Template analysis results comparing *baseline* to *baseline + Sgr dSph* models. Columns (1) - (3) specify the baseline templates used for Galactic hadronic / bremsstrahlung emission, inverse Compton emission, and the Fermi Bubbles, respectively. Column (4) specifies source templates describing the Sgr dSph (see Methods for details). Columns (5) and (6) give the log likelihood for the baseline model (without the Sgr dSph) and the baseline + Sgr dSph model, and columns (7) and (8) give the test statistic with which the baseline + Sgr dSph model is preferred, and the corresponding statistical significance of that preference. The improvement in TS going from {HD, 3D, U, Model I} to {HD, 3D, S, Model I} is $\Delta TS = 854.2$, equivalent to 28.0σ . Note that Sgr dSph model IV – which generates a statistically insignificant improvement to the baseline for one particular combination in the last cluster – is the sparsest stellar template, containing only 675 stars.

206 **Methods**

207 Our analysis pipeline consists of three steps: (1) data and template selection, (2) fitting, and (3) spectral modeling.

208 **Data and template selection**

209 We use eight years of LAT data, selecting `Pass 8 UltraCleanVeto` class events in the energy range from 500 MeV to
210 177.4 GeV. We choose the limit at low energy to mitigate both the impact of the leakage from the Earth's limb γ -ray and the
211 increasing width of the point-spread function at lower energies. We spatially bin the data to a resolution of 0.2° , and divide it
212 into 15 energy bins; the 13 lowest-energy of these are equally spaced in log energy, while the 2 highest-energy are twice that
213 width in order to improve the signal to noise. We select data obtained over the same observation period as that used in the
214 construction of the Fourth Fermi Catalogue (4FGL)[29] (August 4, 2008 to August 2, 2016). The region of interest (ROI) of
215 our analysis is a square region defined by $-45^\circ \leq b \leq -5^\circ$, and $30^\circ \geq \ell \geq -10^\circ$ (Figure 1). This sky region fully contains
216 the Fermi cocoon substructure but avoids the Galactic plane ($|b| \leq 5^\circ$) where uncertainties are largest. Because the ROI is of
217 modest size, we allow the Galactic diffuse emission (GDE) templates greater freedom to reproduce potential features in the
218 data. We carry out all data reduction and analysis using the standard FERMITOOLS v1.0.1¹ software package. We model the
219 performance of the LAT with the `P8R3_ULTRACLEANVETO_V2` Instrument Response Functions (IRFs).

220 We fit the spatial distribution of the ROI data as the sum of a series of templates for different components of the emission.
221 For all the templates we consider, we define a “baseline” model that includes only known point and diffuse emission sources,
222 to which we compare a “baseline + Sgr dSph” model that includes those templates plus the Sgr dSph. Our baseline models,
223 following the approach of Ref. [30], contain the following templates: (1) diffuse isotropic emission, (2) point sources, (3)
224 emission from the Sun and Moon, (4) Loop I, (5) the Galactic Centre Excess, (6) Galactic cosmic ray-driven hadronic and
225 bremsstrahlung emission, (7) inverse Compton emission, and (8) the *Fermi* Bubbles; baseline + Sgr dSph models also include a
226 Sgr dSph template.

227 Our templates for the first five emission sources are straightforward, and we adopt a single template for each of them
228 throughout our analysis. Since our data selection is identical to that used to construct the 4FGL, we adopt the standard isotropic
229 background and point source models provided as part of the catalogue [29], `iso_P8R3_ULTRACLEANVETO_V2_v1.txt`,
230 and `gll_psc_v20.fit`, respectively; the latter includes 177 γ ray point sources within our ROI. We similarly adopt the
231 standard Sun and Moon templates provided. For the foreground structure Loop I, we adopt the model of Ref. [31]. Finally,
232 given that the low-latitude boundary of our ROI overlaps with the spatial tail of the Galactic Centre Excess (GCE), we include
233 the ‘Boxy Bulge’ template of Ref. [32], which has been shown [16–18] to provide a good description of the observed GCE
234 away from the nuclear Bulge region (which is outside our ROI). The inclusion of this template in our ROI model has only a
235 small impact on our results.

236 The remaining templates require more care. The dominant source of γ -rays within the ROI is hadronic and bremsstrahlung

¹<https://github.com/fermi-lat/Fermitools-conda/wiki>

237 emission resulting from the interaction of Milky Way cosmic ray (CR) protons and electrons with interstellar gas; the emission
238 rate is proportional to the product of the gas density and the CR flux. We model this distribution using three alternative
239 approaches. Our preferred approach follows that described in Ref. [16]. We assume that the spatial distribution of γ -ray
240 emission traces the gas distribution from the hydrodynamical model of Ref. [33], which gives a more realistic description
241 of the inner Galaxy than alternatives. To normalise the emission, we divide the Galaxy into four rings spanning the radial
242 ranges $0 - 3.5$ kpc, $3.5 - 8.0$ kpc, $8.0 - 10.0$ kpc, and $10.0 - 50.0$ kpc, within which we treat the emission per unit gas mass in
243 each of our 15 energy bins as a constant to be fit. We refer to the template produced in this way as the “HD” model. Our first
244 alternative is to use the same procedure of dividing the Galaxy into rings, but describe the gas distribution within those rings
245 using a template constructed from interpolated maps of Galactic H I and H₂, following the approach described in Appendix B
246 of Ref. [34]; we refer to this as the “Interpolated” approach. Our third alternative, the “GALPROP” model, is the SA50 model
247 described by Ref. [35], which prescribes the full-sky hadronic CR emission distribution.

248 We similarly need a model for diffuse, Galactic IC emission – the second largest source of background – which is a product
249 of the CR electron flux and the interstellar radiation field (ISRF). As with hadronic emission, we consider four alternative
250 distributions. Our default choice is the SA50 model described by Ref. [35], which includes 3D models for the ISRF [36]. We
251 therefore refer to this as the “3D” model. However, unlike in Ref. [35], we use this model only to obtain the spatial distribution
252 of the emission, not its normalisation or energy dependence. Instead, we obtain these in the same way as for our baseline
253 hadronic emission model, i.e., we divide the Galaxy into four rings and leave the total amount of emission in each ring at
254 each energy as a free parameter to be fit to the data; this approach reduces the sensitivity of our results to uncertainties in the
255 electron injection spectrum and ISRF normalisation. Our three alternatives to this are models “2D A”, “2D B”, and “2D C”,
256 corresponding to models A, B, and C as described by Ref. [37], which model IC emission over the full sky under a variety of
257 assumptions about CR injection and propagation, but rely on a 2D model for the ISRF.

258 The final component of our baseline template is a model for the Fermi Bubbles themselves, which are one of the strongest
259 sources of foreground emission in high latitude regions of the ROI. The FBs are themselves defined as highly statistically-
260 significant and spatially-coherent residuals in the inner Galaxy that remain once other sources are modelled out in all-sky
261 γ -ray analyses. The FBs are not reliably traced by emission at any other wavelength, so we do not have an *a priori* model
262 with which to guide the construction of a spatial template of these structures. However, one characteristic that renders the
263 FBs distinct from other large angular scale diffuse γ -ray structures is their hard γ -ray spectrum. Indeed, the state-of-the-art,
264 *structured* spatial template for them generated by the *Fermi* Collaboration[2] – the templates one would normally employ in
265 large ROI, inner Galaxy *Fermi*-LAT analyses – were constructed using a spectral component analysis. That study recovered
266 a number of regions of apparent substructure within the solid angle of the FBs, most notably substructure overlapping the
267 previously-discovered[4, 5] “cocoon” which, as we have discussed here, is largely coincident with the Sgr dSph. Of course, a
268 potential issue with constructing a phenomenological, spectrally-defined model for the FBs is that, if there happens to be an
269 extended, spectrally-similar source coincident with the FBs, it will tend to be incorporated into the template. For this reason

270 Ref. [2] suggest using a flat FB template when searching for new structures. Despite this proposal, our default analysis uses
 271 the more conservative choice of a structured FB template. However, we also run tests using an unstructured template for
 272 comparison, and to understand the systematic uncertainties associated with the choice of template. We refer to these two cases
 273 as the “U” (Unstructured) and “S” (Structured) FB templates, respectively.

274 Finally, our baseline + Sgr dSph models require a template for the Sgr dSph. Our templates trace the distribution of bright
 275 stars in the dwarf, which we construct from five alternative stellar catalogues, all based on different selections from *Gaia* Data
 276 Release 2; we refer to the resulting templates as models I - V, and show them in E.D. [Figure 4](#). Full details on how we construct
 277 each of these templates are provided in the S.I. Model I, our default choice, comes from the catalogue of 2.6×10^5 Sgr dSph
 278 candidate member stars from Ref. [7]; the majority of the catalogue consists of red clump stars. Model II uses the catalogue
 279 of RR Lyrae stars in the Sagittarius Stream from Ref. [38], which we have down-selected to a sample of 2369 stars whose
 280 kinematics are consistent with being members of the Sgr dSph itself. Model III uses the catalogue of 1.31×10^4 RR Lyrae stars
 281 belonging to the Sgr dSph provided by Ref. [39]. Finally, models IV and V come from the nGC3 and Strip catalogues of RR
 282 Lyrae stars from Ref. [40]; the former contains 675 stars with higher purity but lower completeness, while the latter contains
 283 4812 stars of higher completeness but lower purity.

284 Fitting procedure

Our fitting method follows that introduced in Refs. [16, 18], and treats each of the 15 energy bins as independent, thereby removing the need to assume any particular spectral shape for each component and allowing the spectra to be determined solely by the data. Our data to be fit consist of the observed γ -ray photon counts in each spatial pixel i and energy bin n , which we denote $\Phi_{n,i,\text{obs}}$, where n goes from 1 to 15, and the index i runs over the positions (ℓ_i, b_i) of all spatial pixels within the ROI. For a given choice of template, we write the corresponding model-predicted γ -ray counts as $\Phi_{n,i,\text{mod}} = \sum_c \mathcal{N}_{n,c} R_{n,i} \Phi_{c,i}$, where $R_{n,i}$ is the instrument response for each pixel and energy bin (computed assuming an E^{-2} spectrum within the bin), and $\Phi_{c,i}$ is the value of template component c evaluated at pixel i ; for baseline models, we have a total of 8 components, while for baseline + Sgr dSph models we have 9. Note that $\Phi_{c,i}$ is a function of i but not of n , i.e., we assume that the spatial distribution of each template component is the same at all energies, except for the IC templates, for which an energy-dependent morphology is predicted by our GALPROP simulations. Without loss of generality we further normalise each template component as $\sum_i \Phi_{c,i} = 1$, in which case $\mathcal{N}_{n,c}$ is simply the total number of photons contributed by component c in energy bin n , integrated over the full ROI; the values of $\mathcal{N}_{n,c}$ are the parameters to be fit. We find the best fit by maximising the usual Poisson likelihood function

$$\ln \mathcal{L}_n = \sum_i \frac{\Phi_{n,i,\text{mod}}^{\Phi_{n,i,\text{obs}}} e^{-\Phi_{n,i,\text{mod}}}}{\Phi_{n,i,\text{obs}}!}, \quad (1)$$

285 using the `pylikelihood` routine, the standard maximum-likelihood method in `FermiTools`. Note that, since each energy
 286 bin n is independent, we carry out the likelihood maximisation bin-by-bin.

We perform all fits in pairs, one for a baseline model containing only known emission sources, and one for a baseline + Sgr dSph model containing the same known sources plus a component tracing the Sgr dSph. The set of paired fits we perform in this manner is shown in [Table 1](#). We compare the quality of these baseline and baseline + Sgr dSph fits by defining the test statistic $\text{TS}_n = -2 \ln(\mathcal{L}_{n,\text{base}}/\mathcal{L}_{n,\text{base+Sgr}})$; the total test statistic for all energy bins is simply $\text{TS} = \sum_n \text{TS}_n$. We can assign a p -value to a particular value of the TS by noting that baseline + Sgr dSph models have 15 additional degrees of freedom compared to baseline models: the value of $\mathcal{N}_{n,c}$ for the component c corresponding to the Sgr dSph, evaluated at each of the 15 energy bins. In this case, the mixture distribution formula gives[[16](#)]

$$p(\text{TS}) = 2^{-N} \left[\delta(\text{TS}) + \sum_{n=1}^N \binom{n}{k} \chi_n^2(\text{TS}) \right], \quad (2)$$

where $N = 15$ is the difference in number of degrees of freedom, $\binom{n}{k}$ is the binomial coefficient, δ is the Dirac delta function, and χ_n^2 is the usual χ^2 distribution with n degrees of freedom. The corresponding statistical significance (in σ units) is[[16](#)]:

$$\text{Number of } \sigma \equiv \sqrt{\text{InverseCDF}(\chi_1^2, \text{CDF}[p(\text{TS}), \hat{\text{TS}}])}, \quad (3)$$

where (InverseCDF) CDF is the (inverse) cumulative distribution function and the first argument of each of these functions is the distribution function, the second is the value at which the CDF is evaluated, and the total TS is denoted by $\hat{\text{TS}}$. For 15 extra degrees of freedom, a 5σ detection corresponds to $\text{TS} = 46.1$. We report values of $\mathcal{L}_{\text{base}}$, $\mathcal{L}_{\text{base+Sgr}}$, TS , and the significance level for all the templates we try in [Table 1](#).

A final step in our fitting chain is to assess the uncertainties. For our default choice of baseline + Sgr dSph model (first row in [Table 1](#)), our maximum likelihood analysis returns the central value $\mathcal{N}_n^{\text{def}}$ on the total γ -ray flux in the n th energy bin attributed to the Sgr dSph, and also yields an uncertainty $\sigma_{\mathcal{N},n}^{\text{def}}$ on this quantity. This represents the statistical error arising from measurement uncertainties. However, there are also systematic uncertainties stemming from our imperfect knowledge of the templates characterising the other emission sources. To estimate these, we examine the five alternative models listed in [Table 1](#) as “Alternative background templates”, where we use different templates for the hadronic plus bremsstrahlung and inverse Compton backgrounds. Each of these models m also returns a central value \mathcal{N}_n^m and an uncertainty $\sigma_{\mathcal{N},n}^m$ on the Sgr dSph flux. We use the uncertainty-weighted dispersion of these models as an estimate of the systematic uncertainty (e.g.,ref. [[41](#)]):

$$\delta \mathcal{N}_n = \sqrt{\frac{1}{\sum_m (\sigma_{\mathcal{N},n}^m)^{-2}} \sum_m (\sigma_{\mathcal{N},n}^m)^{-2} (\mathcal{N}_n^{\text{def}} - \mathcal{N}_n^m)^2}, \quad (4)$$

where the sums run over the $m = 6 - 1$ alternative models. We take the total uncertainty on the Sgr dSph flux in each energy bin to be a quadrature sum of the systematic and statistical uncertainties, i.e., $(\sigma_{\mathcal{N},n}^{\text{def,tot}})^2 = (\sigma_{\mathcal{N},n}^{\text{def}})^2 + \delta \mathcal{N}_n^2$. We plot the central values and uncertainties of the fluxes for the default model derived in this manner in [Figure 2](#).

We have carried out several validation tests of this pipeline, which we describe in the Supplementary Information (SI).

We model the observed Sgr dSph γ -ray spectrum as a combination of prompt magnetospheric MSP emission and IC emission from e^\pm escaping MSP magnetospheres. We construct this model as follows. The prompt component is due to curvature radiation from e^\pm in the magnetosphere. The e^\pm energy distribution can be approximated as an exponentially-truncated power law [22, 42]

$$\frac{dN_{\text{MSP},e^\pm}}{dE_{e^\pm}} \propto E_{e^\pm}^{\gamma_{\text{MSP}}} \exp\left(-\frac{E_{e^\pm}}{E_{\text{cut},e^\pm}}\right), \quad (5)$$

and curvature radiation from these particles has a rate of photon emission per unit energy per unit time

$$\frac{d\dot{N}_{\gamma,\text{prompt}}}{dE_\gamma} = \mathcal{N}(L_{\gamma,\text{prompt}}) E_\gamma^\alpha \exp\left(-\frac{E_\gamma}{E_{\text{cut,prompt}}}\right), \quad (6)$$

where E_γ is the photon energy, $\mathcal{N}(L_{\gamma,\text{prompt}})$ is a normalisation factor chosen so that the prompt component has total luminosity $L_{\gamma,\text{prompt}}$, the index α is related to that of the e^\pm distribution by $\alpha = (\gamma_{\text{MSP}} - 1)/3$, and the photon cutoff energy is related to the e^\pm cutoff energy by [24]

$$E_{\text{cut,prompt}} = \frac{3\hbar c}{2\rho_c} \left(\frac{E_{\text{cut},e^\pm}}{m_e}\right)^3 \simeq 2.0 \text{ GeV} \left(\frac{\rho_c}{30 \text{ km}}\right)^{-1} \left(\frac{E_{\text{cut},e^\pm}}{3 \text{ TeV}}\right)^3 \quad (7)$$

296 where m_e is the electron mass, ρ_c is the radius of curvature of the magnetic field lines, and the other symbols have the usual
297 meanings. Given the rather small magnetospheres, we expect ρ_c to be a small multiple of the ~ 10 km neutron star characteristic
298 radius; henceforth we set $\rho_c = 30$ km. Empirically, $L_{\gamma,\text{prompt}}$ is $\sim 10\%$ of the total MSP spin-down power [42].

A larger proportion of the spin-down power goes into a wind of e^\pm escaping the magnetosphere. In the ultra-low density and magnetic field environment of the Sgr dSph, the only significant loss mechanism for these e^\pm is IC emission, resulting in a steady-state e^\pm energy distribution

$$\frac{dN_{e^\pm}}{dE_{e^\pm}} \propto E_{e^\pm}^\gamma \exp\left(-\frac{E_{e^\pm}}{E_{\text{cut},e^\pm}}\right), \quad (8)$$

where $\gamma = \gamma_{\text{MSP}} - 1$. We compute the IC photon distribution produced by these particles following ref. [43], assuming that ISRF of the Sgr dSph is the sum of the CMB and a subdominant dilute stellar blackbody radiation field with colour temperature 3500 K and dilution factor of 7.0×10^{-15} (giving energy density 0.005 eV cm^{-3}); these choices are those expected for a spherical region of radius 2.6 kpc and stellar luminosity $2 \times 10^8 L_\odot$, the approximate parameters of the Sgr dSph. This yields an IC spectrum

$$\frac{d\dot{N}_{\gamma,\text{IC}}}{dE_\gamma} = \mathcal{N}(L_{\gamma,\text{IC}}) F(\gamma, E_{\text{cut},e^\pm}), \quad (9)$$

299 where $\mathcal{N}(L_{\gamma, \text{IC}})$ is again a normalisation chosen to ensure that the total IC luminosity is $L_{\gamma, \text{IC}}$, and $F(\gamma, E_{\text{cut}, e^\pm})$ is the
 300 functional form given by equation 14 of ref. [43], which depends on the e^\pm spectral index γ and cutoff energy E_{cut, e^\pm} .

Combining the prompt and IC components, we may therefore write the complete emission spectrum as

$$\frac{d\dot{N}_\gamma}{dE_\gamma} = \mathcal{N}(L_{\gamma, \text{prompt}}) E_\gamma^\alpha \exp\left(-\frac{E_\gamma}{E_{\text{cut}, \text{prompt}}}\right) + \mathcal{N}(L_{\gamma, \text{IC}}) F(\gamma, E_{\text{cut}, e^\pm}). \quad (10)$$

301 This model is characterised by four free parameters: the total prompt plus IC luminosity $L_{\gamma, \text{tot}} = L_{\gamma, \text{prompt}} + L_{\gamma, \text{IC}}$, the ratio of
 302 the prompt and IC luminosities $f = L_{\gamma, \text{prompt}}/L_{\gamma, \text{IC}}$, the spectral index α of the prompt component (which in turn fixes the other
 303 two spectral indices γ_{MSP} and γ), and the cutoff energy for the prompt component $E_{\text{cut}, \text{prompt}}$ (which then fixes the e^\pm cutoff
 304 energy E_{cut, e^\pm}).

305 We fit the observed Sgr dSph spectrum to this model using a standard χ^2 minimisation, using the combined statistical
 306 plus systematic uncertainty. We obtain an excellent fit: the minimum χ^2 is 7.7 for 15 (data points) - 4 (fit parameters) = 11
 307 (degrees of freedom, dof) or a reduced χ^2 of 0.70. We report the best-fitting parameters in E.D. [Table 2](#), and plot the result
 308 best-fit spectra over the data in [Figure 2](#); we show the best-fit estimate (with $\pm 1\sigma$ confidence region) for the magnetospheric
 309 luminosity per stellar mass of the Sgr dSph MSPs in [Figure 3](#).

310 We also carry out an additional consistency check, by comparing our best-fit parameters describing the prompt emission – α
 311 and $E_{\text{cut}, \text{prompt}}$ – to direct measurements of the prompt component from nearby, resolved MSPs [22, 42], and to measurements
 312 of GCs, whose emission is likely dominated by unresolved MSPs [22]. We carry out this comparison in E.D. [Figure 11](#). In
 313 this figure, we show joint confidence intervals on α and $E_{\text{cut}, \text{prompt}}$ from our fit. For comparison, we construct confidence
 314 intervals for α and $E_{\text{cut}, \text{prompt}}$ from observations using the sample of ref. [22], who fit the prompt emission from 40 GCs and
 315 110 individually-resolved MSPs. We draw 100,000 Monte Carlo samples from these fits, treating the stated uncertainties as
 316 Gaussian, and construct contours in the $(E_{\text{cut}, \text{prompt}}, \alpha)$ plane containing 68%, 95%, and 99% of the sample points. As the plot
 317 shows, the confidence region from our fit is fully consistent with the confidence regions from the observations, indicating that
 318 our best-fit parameters are fully consistent those typically observed for MSPs and GCs.

319 **Methods References**

- 320 29. Abdollahi, S. et al. Fermi Large Area Telescope Fourth Source Catalog. *Astrophys. J. Suppl.* **247**, 33. doi:[10.3847/1538-4365/ab6bcb](https://doi.org/10.3847/1538-4365/ab6bcb) (2020).
- 321 30. Abazajian, K. N., Horiuchi, S., Kaplinghat, M., Keeley, R. E. & Macias, O. Strong constraints on thermal relic dark
323 matter from Fermi-LAT observations of the Galactic Center. *Phys. Rev. D* **102**, 043012. doi:[10.1103/PhysRevD.102.043012](https://doi.org/10.1103/PhysRevD.102.043012) (2020).
- 324 31. Wolleben, M. A New Model for the Loop I (North Polar Spur) Region. *Astrophys. J.* **664**, 349–356. doi:[10.1086/518711](https://doi.org/10.1086/518711) (2007).
- 325 32. Freudenreich, H. T. A COBE Model of the Galactic Bar and Disk. *Astrophys. J.* **492**, 495–510. doi:[10.1086/305065](https://doi.org/10.1086/305065) (1998).
- 326 33. Pohl, M., Englmaier, P. & Bissantz, N. Three-Dimensional Distribution of Molecular Gas in the Barred Milky Way.
329 *Astrophys. J.* **677**, 283–291. doi:[10.1086/529004](https://doi.org/10.1086/529004) (2008).
- 330 34. Ackermann, M. et al. Fermi-LAT Observations of the Diffuse γ -Ray Emission: Implications for Cosmic Rays and the
332 Interstellar Medium. *Astrophys. J.* **750**, 3. doi:[10.1088/0004-637X/750/1/3](https://doi.org/10.1088/0004-637X/750/1/3) (2012).
- 333 35. Jóhannesson, G., Porter, T. A. & Moskalenko, I. V. The Three-dimensional Spatial Distribution of Interstellar Gas
334 in the Milky Way: Implications for Cosmic Rays and High-energy Gamma-ray Emissions. *Astrophys. J.* **856**, 45.
335 doi:[10.3847/1538-4357/aab26e](https://doi.org/10.3847/1538-4357/aab26e) (2018).
- 336 36. Porter, T. A., Johannesson, G. & Moskalenko, I. V. High-Energy Gamma Rays from the Milky Way: Three-Dimensional
337 Spatial Models for the Cosmic-Ray and Radiation Field Densities in the Interstellar Medium. *Astrophys. J.* **846**, 67.
338 doi:[10.3847/1538-4357/aa844d](https://doi.org/10.3847/1538-4357/aa844d) (2017).
- 339 37. Ackermann, M. et al. The Spectrum of Isotropic Diffuse Gamma-Ray Emission between 100 MeV and 820 GeV.
340 *Astrophys. J.* **799**, 86. doi:[10.1088/0004-637X/799/1/86](https://doi.org/10.1088/0004-637X/799/1/86) (2015).
- 341 38. Ibata, R. et al. A Panoramic Landscape of the Sagittarius Stream in Gaia DR2 Revealed with the STREAMFINDER
342 Spyglass. *Astrophys. J. Lett.* **891**, L19. doi:[10.3847/2041-8213/ab77c7](https://doi.org/10.3847/2041-8213/ab77c7) (2020).
- 343 39. Iorio, G. & Belokurov, V. The shape of the Galactic halo with Gaia DR2 RR Lyrae. Anatomy of an ancient major merger.
344 *Mon. Not. R. Astron. Soc.* **482**, 3868–3879. doi:[10.1093/mnras/sty2806](https://doi.org/10.1093/mnras/sty2806) (2019).
- 345 40. Ramos, P. et al. Full 5D characterisation of the Sagittarius stream with Gaia DR2 RR Lyrae. *Astron. Astrophys.* **638**, A104.
346 doi:[10.1051/0004-6361/202037819](https://doi.org/10.1051/0004-6361/202037819) (2020).
- 347 41. Ackermann, M. et al. The Search for Spatial Extension in High-latitude Sources Detected by the Fermi Large Area
348 Telescope. *Astrophys. J. Suppl.* **237**, 32. doi:[10.3847/1538-4365/aacdf7](https://doi.org/10.3847/1538-4365/aacdf7) (2018).

- 349 42. Abdo, A. A. et al. The Second Fermi Large Area Telescope Catalog of Gamma-Ray Pulsars. *Astrophys. J. Suppl.* **208**, 17.
350 doi:[10.1088/0067-0049/208/2/17](https://doi.org/10.1088/0067-0049/208/2/17) (2013).
- 351 43. Khangulyan, D., Aharonian, F. A. & Kelner, S. R. Simple Analytical Approximations for Treatment of Inverse Compton
352 Scattering of Relativistic Electrons in the Blackbody Radiation Field. *Astrophys. J.* **783**, 100. doi:[10.1088/0004-637X/783/2/100](https://doi.org/10.1088/0004-637X/783/2/100) (2014).
353

354 **Acknowledgements**

355 RMC acknowledges support from the Australian Government through the Australian Research Council, award DP190101258
356 (shared with MRK) and hospitality from the Virginia Institute of Technology, the Max-Planck Institut für Kernphysik, and
357 the GRAPPA Institute at the University of Amsterdam supported by the Kavli IPMU at the University of Tokyo. O.M. is
358 supported by the GRAPPA Prize Fellowship and JSPS KAKENHI Grant Numbers JP17H04836, JP18H04340, JP18H04578,
359 and JP20K14463. This work was supported by World Premier International Research Centre Initiative (WPI Initiative), MEXT,
360 Japan. ADM acknowledges support from the Australian Government through a Future Fellowship from the Australian Research
361 Council, award FT160100206. M.R.K. acknowledges support from the Australian Government through the Australian Research
362 Council, award DP190101258 (shared with RMC) and FT180100375. The work of S.H. is supported by the U.S. Department of
363 Energy Office of Science under award number DE-SC0020262 and NSF Grant No. AST-1908960 and No. PHY-1914409. The
364 work of DS is supported by the U.S. Department of Energy Office of Science under award number DE-SC0020262. T.V. and
365 A.R.D. acknowledge the support of the Australian Research Council's Centre of Excellence for Dark Matter Particle Physics
366 (CDM) CE200100008. AJR acknowledges support from the Australian Government through the Australian Research Council,
367 award FT170100243. RMC thanks Elly Berkhuijsen, Rainer Beck, Ron Ekers, Matt Roth, and Thomas Siegert for useful
368 communications.

369 **Author contributions statement**

370 R.M.C. initiated the project and led the spectral analysis and theoretical interpretation. O.M constructed the astrophysical
371 templates, designed the analysis pipeline, and performed the data analysis of γ ray observations. D.M., M.R.K., C.G., R.J.T.,
372 F.A., J.A.H., S.A., S.H., A.G., M.R., L.F., and A.R. provided theoretical insights and interpretation, and advice about statistical
373 analysis. T.V. and A.R.D. provided insights on the expected distribution of dark matter. R-Z.Y. performed an initial γ -ray
374 data analysis. M.D.F helped with radio data. The main text was written by RMC, MRK, and O.M. and the Methods section
375 was written by O.M., R.M.C., and MRK. All authors were involved in the interpretation of the results and all reviewed the
376 manuscript.

377 **Additional information**

378 To include, in this order: **Accession codes** (where applicable); .

379 **Competing interests**

380 The authors declare no competing interests.

quantity	best-fit	68% c.l.	units	literature value(s)
$l_0 \equiv L_{\gamma,\text{tot}}/M_\star$	5.2	[4.4, 6.0]	$10^{28} \text{ erg/s}/M_\odot$	$\sim (1 - 10)$ [23]
$f = L_{\gamma,\text{prompt}}/L_{\gamma,\text{IC}}$	0.83	[0.59, 1.3]	—	~ 0.1 [23]
α	0.039	[-0.38, 0.62]	—	-0.88 ± 0.44 [22]
$E_{\text{cut,prompt}}$	1.0	[0.74, 1.3]	GeV	$1.91^{+0.85}_{-0.59} \pm 0.44$ [22]

Table 2. Best fit spectral parameters with $\pm 1\sigma$ confidence regions as determined from χ^2 fitting to the measured γ -ray spectrum of the Sgr dSph. The parameter l_0 is calculated using $M_\star = 10^8 M_\odot$ [8] for the Sgr dSph. See also E.D. Figure 11

381 Extended Data

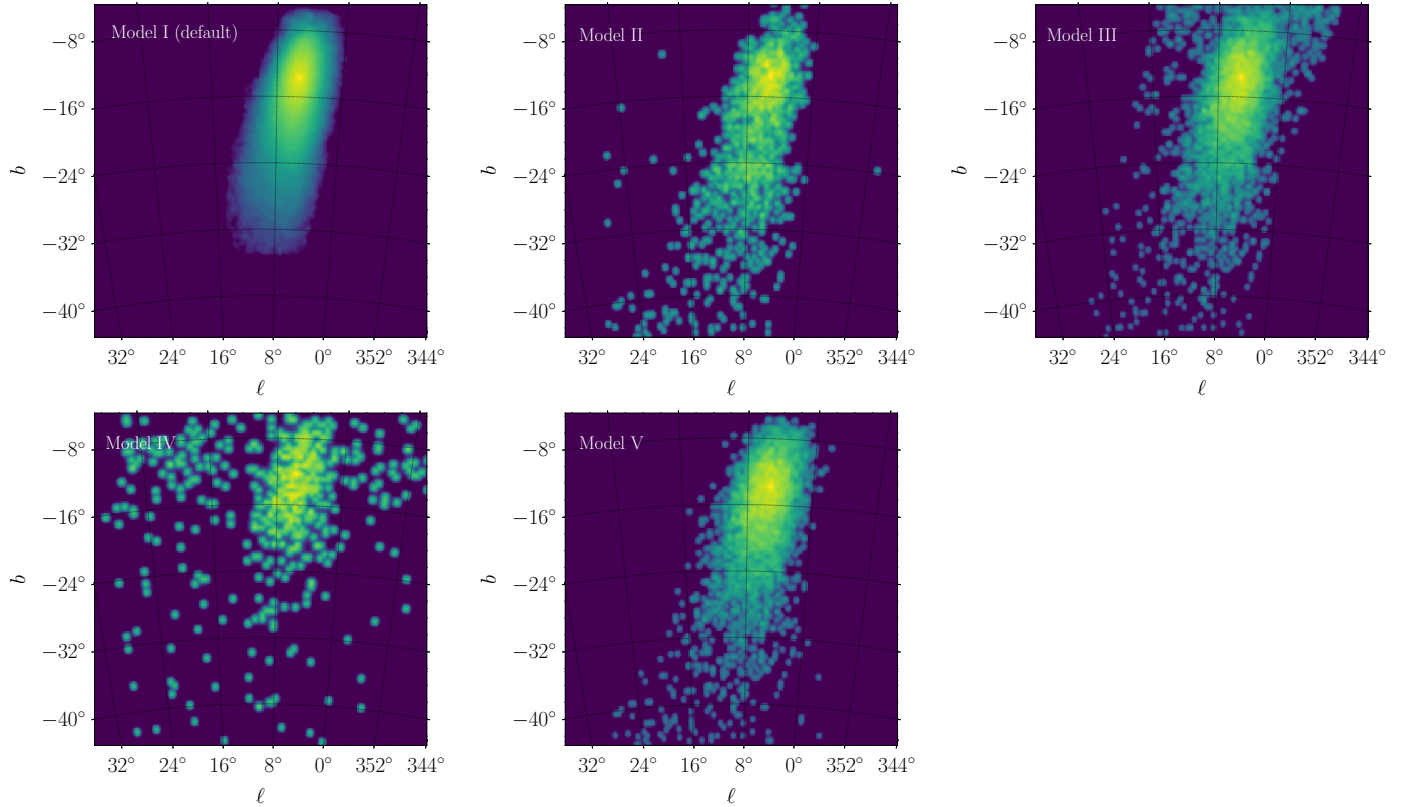


Figure 4. The stellar density templates for the Sgr dSph used in this study. Each map has been normalized, so the units are arbitrary; the color scale is linear. Morphological differences among the templates are due to different stellar candidates (red clump or RR Lyrae), search algorithms, and search target (the dwarf remnant or the stream). Data sources are as follows: Model I, ref. [7]; Model II, ref. [38]; Model III, ref. [39]; Model IV and Model V, ref. [40]. Detailed descriptions of these templates are given in the S.I.

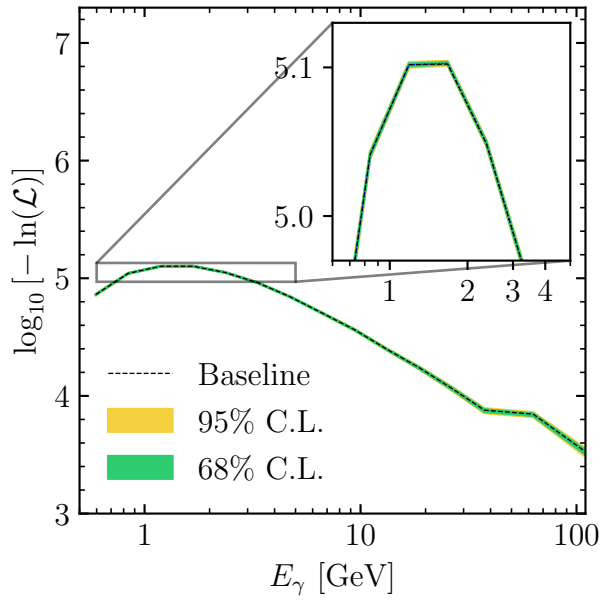


Figure 5. Goodness of fit computation for the best-fitting baseline + Sgr dSph model using our preferred set of templates (first entry in Table 1). The black dotted line shows the log-likelihood $\ln \mathcal{L}$ as a function of energy for the best-fitting model compared to the real *Fermi* observations. The green and yellow bands show the 68% and 95% confidence intervals, respectively, we expect to find for this quantity under the null hypothesis that the best-fitting model is a true representation of the underlying data, and that any residuals between the model and the data are solely the result of photon counting statistics. The fact that the black dotted line lies within these confidence intervals at all energies indicates that we cannot rule out this hypothesis, indicating that our model is as good a fit to the data as could be expected given the finite number of photons that *Fermi* has observed.

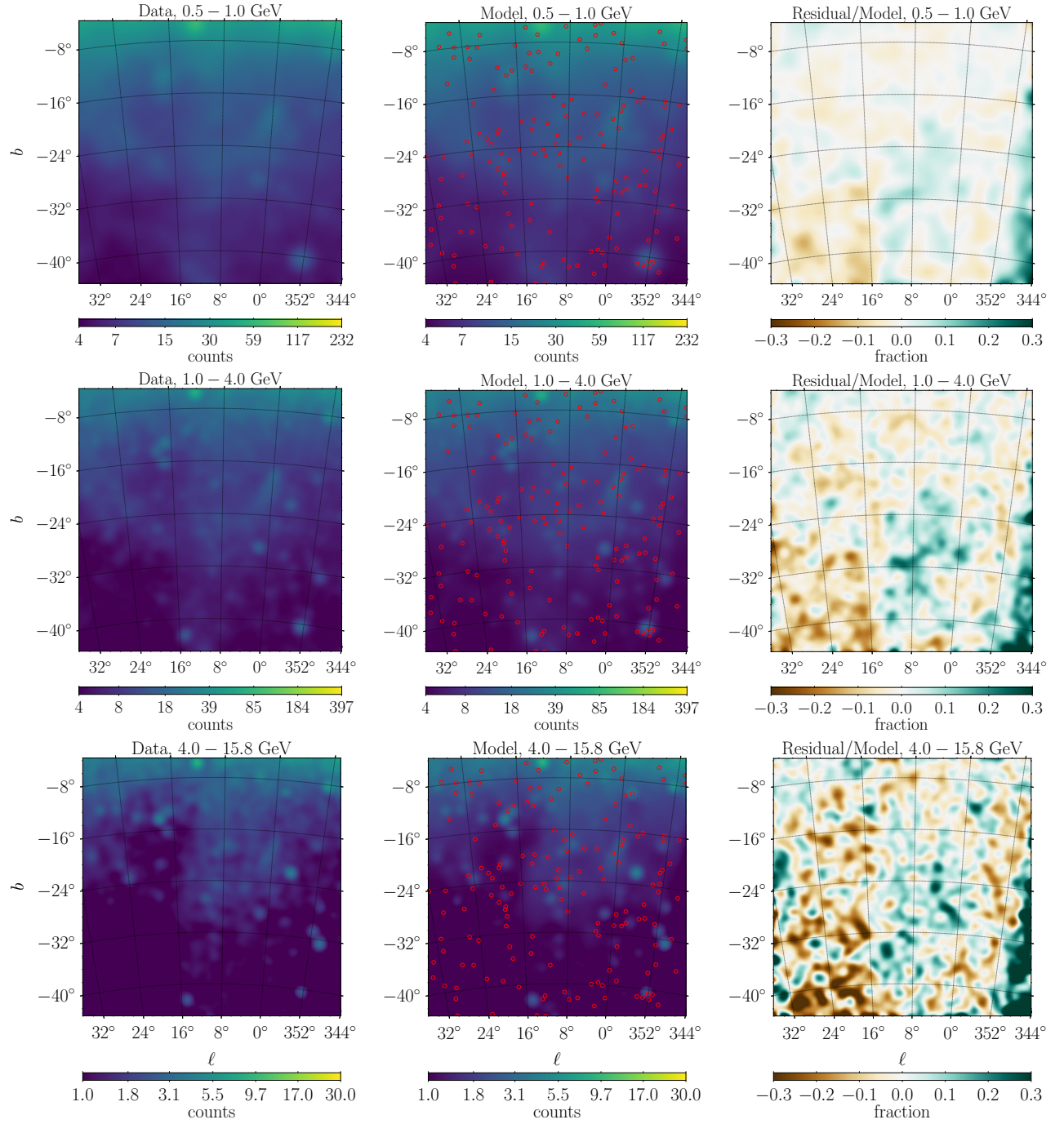


Figure 6. Measured photon counts (left), best-fit baseline + Sgr dSph model (middle), and the fractional residuals ($Data - Model$)/ $Model$ (right). The images were constructed by summing the corresponding energy bins over the energy ranges displayed on top of each panel: [0.5, 1.0] GeV, [1.0, 4.0] GeV, [4.0, 15.8] GeV, from top to bottom. The maps have been smoothed with Gaussian filters of radii 1.0° , 0.8° , and 0.5° for each energy range displayed, respectively (where these angular scales are determined by the *Fermi*-LAT point spread function at the low-edge of the energy interval for the former two, while the latter is determined by the angular resolution of the gas maps). The spectrum of baseline + Sgr dSph model components shown here can be seen in Figure 10. The 4FGL [29] γ -ray point sources included in the baseline model are represented by the red circles.

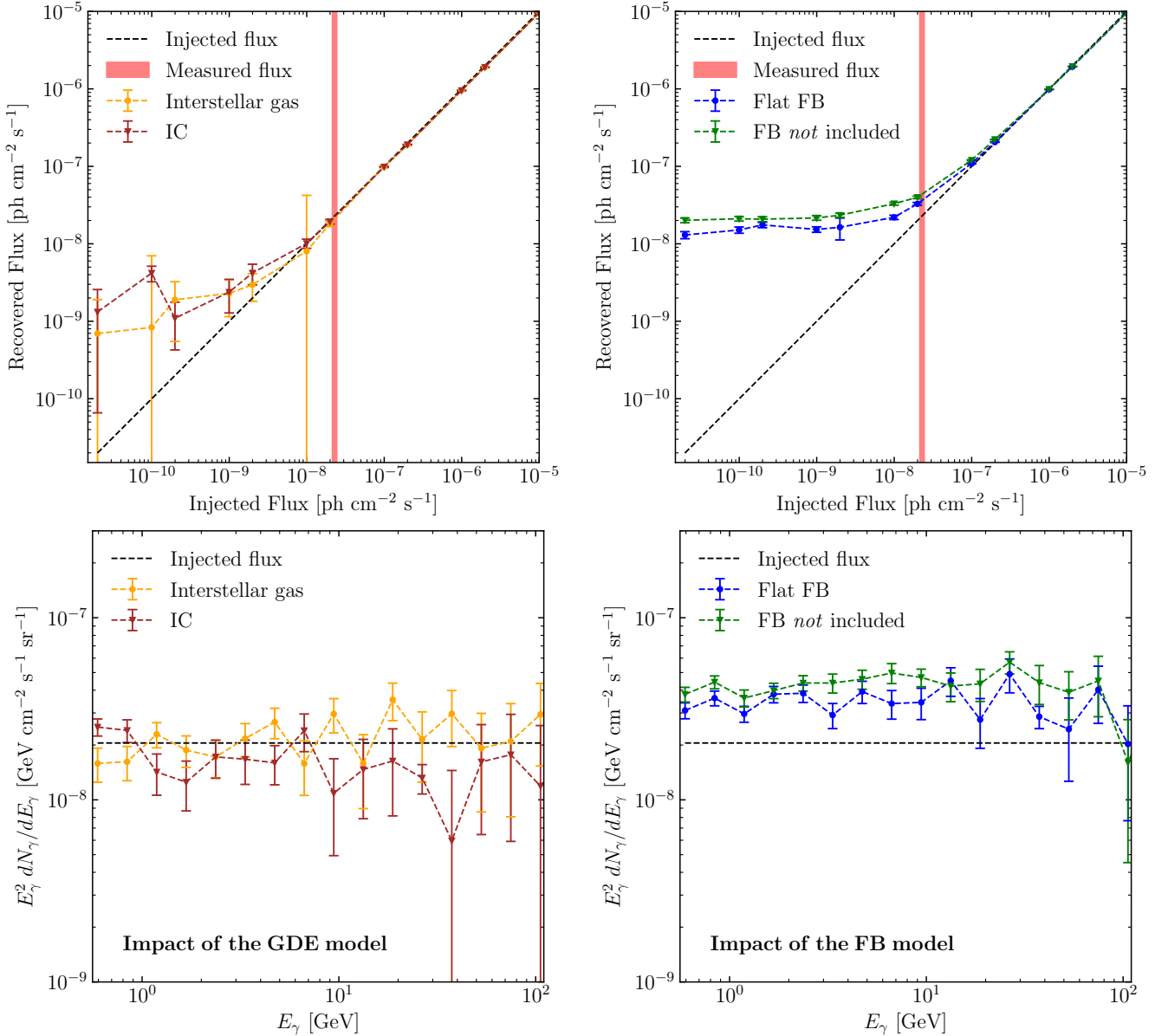


Figure 7. Results from our template mismatch tests. Each of the coloured lines shows the results of a test where we generate synthetic data with one set of templates, and attempt to recover the Sgr dSph in those data using a different set. In the upper two panels, the horizontal axis shows the true, energy-integrated Sgr dSph photon flux in the synthetic data, while the vertical axis shows the value (with error bars) retrieved by our pipeline; the black dashed lines indicate perfect recovery of the input, and the vertical bands show the photon flux we measure for the Sgr dSph in the real *Fermi* data. In the bottom two panels we plot the recovered energy flux in each energy bin, for the case where the injected photon flux most closely matches the real Sgr dSph flux; the black dashed line again shows perfect recovery of the injected signal. The left panels show experiments where we mismatch the Galactic hadronic and IC templates, while the right panels show experiments where we mismatch the FB templates; see Methods for details.

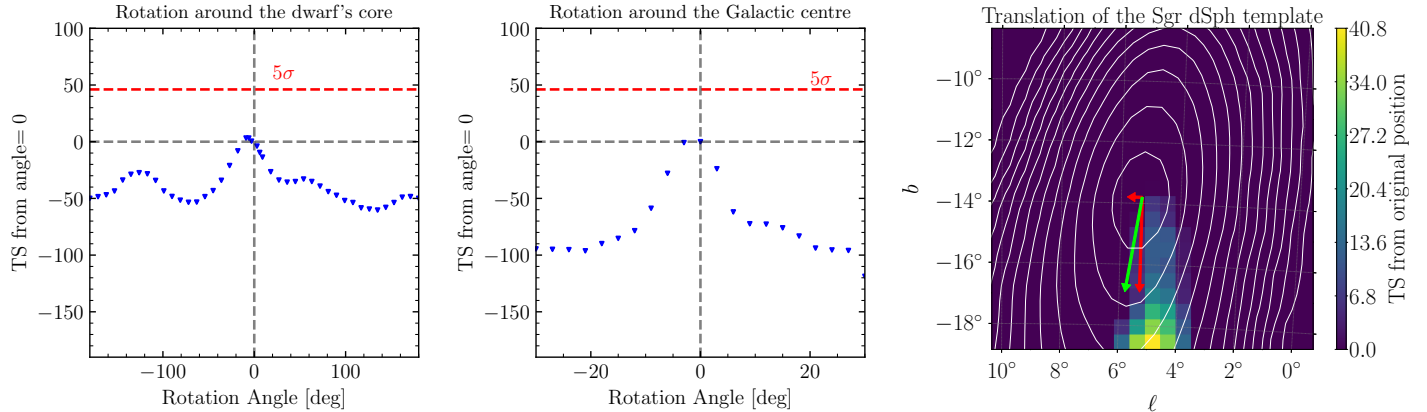


Figure 8. Results of our rotation and translation tests. *Left:* change in TS when repeating the analysis using the default baseline + Sgr dSph model, but with the Sgr dSph rotated about its centre by the indicated angle (blue points); TS values > 0 indicate an improved fit (dashed grey line), with TS = 46.1 corresponding to a 5σ -significant improvement (red dashed line). *Centre:* same as the left panel, but for tests with the Sgr dSph template rotated about the Milky Way centre, rather than its own centre. *Right:* tests for translation of the Sgr dSph template. The true position of the Sgr dSph centre is the center of the plot, and the colour in each pixel indicates the change in TS if we displace the Sgr dSph centre to the indicated position; the maximum shown, at a displacement $\Delta b \approx -4^\circ$, has TS = 40.8, corresponding to 4.5σ significance. For comparison, white contours show the original, unshifted Sgr dSph template, and the green arrow shows the direction anti-parallel to the Sgr dSph's proper motion, back along its past trajectory; red arrows show the projection of the green arrow in the ℓ and b directions.

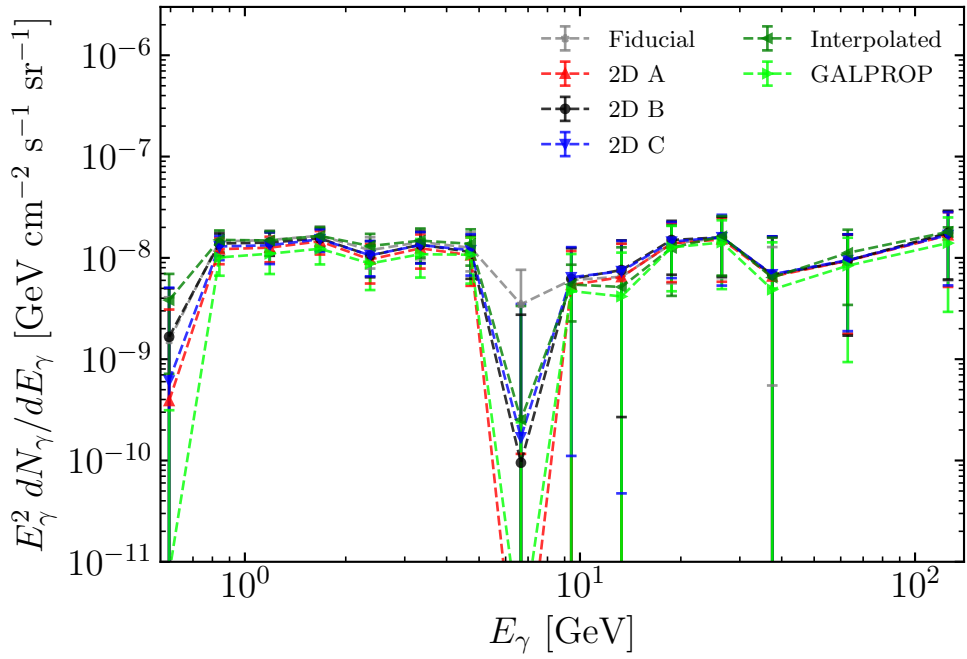


Figure 9. Sgr dSph spectra derived from template analysis using different Galactic diffuse emission models; in all cases the spectrum shown is the flux averaged over the entire ROI, not the flux within the footprint of the Sgr dSph template. The fiducial model is our default choice (first entry in Table 1), while other lines correspond to alternate foregrounds – models 2D A (red), 2D B (black), and 2D C (blue) for the Galactic IC foreground, and models Interpolated (dark green) and GALPROP 3D-gas (light green) for the Galactic hadronic + brehmsstrahlung foreground. The error bars display statistical errors. See Table 1 and text for details.

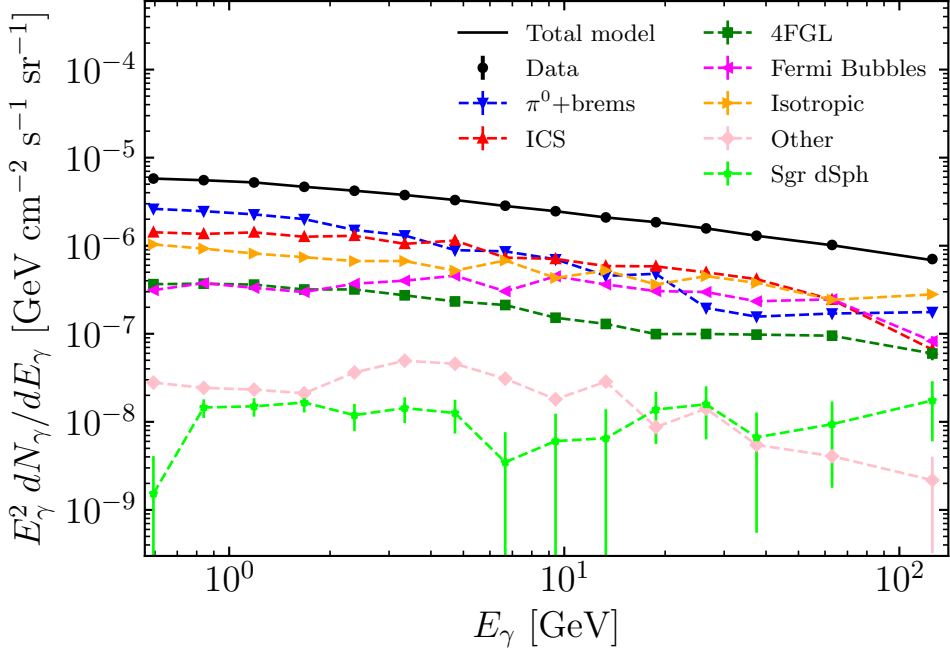


Figure 10. Contribution of each template component to the γ -ray spectrum averaged over the entire ROI, for our default baseline + Sgr dSph model. Components shown are as follows: $\pi^0 + \text{brems}$ is the Galactic hadronic plus bremsstrahlung foreground, ICS is the Galactic inverse Compton foreground, 4FGL indicates point sources from the 4th *Fermi* catalogue, Fermi Bubbles indicates the structured Fermi Bubble template, isotropic is the isotropic γ -ray background, “other” includes the Sun and Moon, Loop I, and the Galactic Centre Excess, and Sgr stream indicates the Sgr dSph.

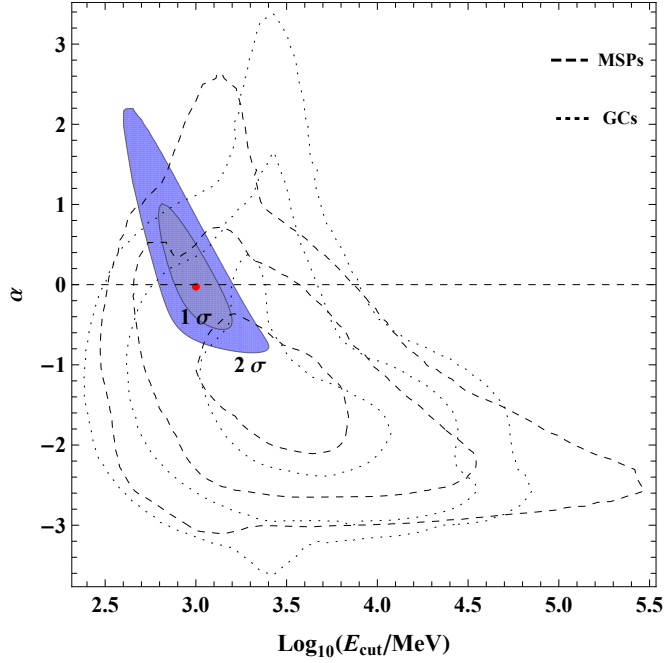


Figure 11. Filled contours indicate the best-fit region for the spectral parameters $E_{\text{cut,prompt}}$ and α that determine the shape of the magnetospheric emission from the Sgr dSph; the outer, coloured region shows the 2σ region, the inner shows the 1σ region, and the red point marks the best fit. The dotted and dashed contours describe the 1 , 2 , and 3 σ confidence regions measured in ref [22] for globular clusters (GCs) and individual resolved MSPs, respectively, constructed from the observations as described in Methods.

382 **Supplementary Information**

383 **1 Chance overlap calculation**

384 In the main text we estimate of the probability of a chance overlap between cocoon γ -ray structure and Sgr dSph to be $\approx 1\%$.
385 This follows simply from noting that the solid angle of the Bubbles is around 0.7 sr [2] and the cocoon covers $\lesssim 20\%$ of this solid
386 angle, so the chance probability for an overlap if these objects were placed randomly on the sky is $\lesssim 0.2 \times 0.7/(4\pi) \sim 0.012$.
387 However, this is a generous upper limit; it does not take into account that, as revealed by the template analysis, there is a much
388 more detailed correspondence between the γ -ray substructure and the stellar distribution not accounted for here. Moreover, the
389 naive 1% estimate does include a ‘look-elsewhere’ correction: the Milky Way is surrounded by satellite galaxies and there
390 are apparently other regions of sub-structure within the Fermi Bubbles. However, not only is the cocoon the brightest and
391 first-discovered region of sub-structure [4], it is also the only region that has been reliably detected by independent analyses
392 [2, 5], and is visibly-evident in independently-produced γ -ray maps [44, 45]. The Sgr dSph is also a special object: it is the
393 brightest MW satellite not yet (prior to this work) detected in γ -rays. (In fact, not only is the Sgr dSph the brightest satellite
394 undiscovered in γ -rays, it is substantially brighter than the next brightest galaxy².) Overall, we have a spatial overlap (and
395 detailed morphological correspondence as argued elsewhere) between the brightest region of substructure within the *Fermi*
396 Bubbles and the Sgr dSph, the second closest, third-most massive, third brightest, and third most angularly extended satellite
397 galaxy of the MW.

398 **2 Construction of the Sgr dSph templates**

399 Here we provide detailed descriptions of how we construct the Sgr dSph templates shown in E.D. [Figure 4](#).

400 **Model I:**

401 We extract this template from the stellar catalogue constructed in Ref. [7], which was derived using photometric and astrometric
402 data from *Gaia* Data Release 2 (DR2), and kinematic measurements from various other surveys. The catalogue consists of
403 a list of 2.6×10^5 candidate member stars of the Sgr dSph remnant, which are reliably separated from the field stars. Every
404 object in the catalogue has an extinction-corrected G-band magnitude larger than 18, and more than half of the objects in this
405 catalogue are classified as red clump stars. Note that Ref. [7] adapted their procedure to reproduce the observed properties of
406 the Sgr dSph remnant, not the stream, which is why the first panel of [Figure 4](#) only shows the dwarf’s remnant.

407 **Model II:**

408 Our second template comes from ref. [38]. Instead of red clump stars, this study selected a sample of RR Lyrae stars from *Gaia*
409 DR2 data, for which distances are accurately measured. Also, rather than focusing on member stars of the Sgr dSph remnant,

²The list of all the MW satellites with apparent magnitude $m < 10$ includes 8 objects, the brightest two, the LMC and SMC, with $m \sim 0.3$ and ~ 2.1 , respectively, are already detected in γ -rays. The next brightest is the Sgr dSph with $m \sim 3$; after that come Fornax, Sculptor, and Leo I with $m \sim 7.3, 8.7$ and 10.0 and angular diameters of $0.24^\circ, 0.51^\circ$ and 0.11° , respectively, which, even assuming they could be detected, would at best only appear marginally extended to *Fermi*-LAT.

410 Ref. [38] used the STREAMFINDER algorithm to single out stars with high probability of belonging to the Sagittarius Stream.
411 By using the kinematic properties of the stars in that study, we constructed a template containing 2369 RR Lyrae stars (cf.
412 [Figure 4](#)) in our ROI. Note that the stellar number count in this map is approximately two orders of magnitude smaller than that
413 in Model I.

414 ***Model III:***

415 Ref. [39] performed an all-sky analysis of RR Lyrae stars (in *Gaia* DR2 data) belonging to globular clusters, dwarf spheroidal
416 galaxies, streams, and the Magellanic Clouds. Our Model III template is a subset of their data identified as belonging to the Sgr
417 dSph, selected to reproduce their Fig. 1 (bottom-right). It includes 1.31×10^4 RR Lyrae stars in our ROI.

418 ***Model IV and Model V:***

419 Ref. [40] developed two empirical catalogues of RR Lyrae stars in *Gaia* DR2 data, which form the basis for our final two
420 templates. The first (Model IV), corresponds to the nGC3 sample, which is characterized for its lower-completeness and higher-
421 purity. This template contains 675 stars in our ROI. The second (Model V), is the Strip sample, containing higher-completeness,
422 but lower purity. The total number of stars in our ROI for this model is 4812.

423

3 Validation tests

424 While our template analysis indicates a strong statistical preference for emission tracing the Sgr dSph, we also carry out four
425 further validation tests to check the robustness of the result.

426 First, we check whether the residuals between the baseline + Sgr dSph source model and the *Fermi* data from our ROI are
427 consistent with the level expected simply as a result of photon counting statistics, using a method similar to that of Ref. [46].
428 Under the null hypothesis that the *Fermi* data are a Poisson draw from our best-fit baseline + Sgr dSph model (i.e., that our
429 model is correct, and any differences between it and the actual data are simply due to shot noise), we can determine the expected
430 distribution of $\ln \mathcal{L}_n$ values via Monte Carlo. For each Monte Carlo trial, we draw a set of mock photon counts $\Phi_{n,i,\text{mock}}$ in
431 each pixel and energy bin from our best-fitting model (multiplied by the instrument response function), and then compute
432 the energy-dependent log-likelihood for this mock data set using the same pipeline we use on the real data. We repeat this
433 procedure 50 times, and plot the distribution of log-likelihood values it produces as the green (68% confidence) and yellow
434 (95% confidence bands) in E.D. [Figure 5](#). These bands represent the expected log likelihood in each energy bin under the null
435 hypothesis. We then compare this to the actual value of $\ln \mathcal{L}_n$ we measure for our model as compared to the real *Fermi* data.
436 The plot shows that our measured log-likelihood falls squarely within the range expected under the null hypothesis, and we
437 therefore conclude that the residuals between our model and the real data are consistent with being solely the result of photon
438 counting statistics.

439 In addition to testing whether the residuals between model and data are consistent with simply being shot noise when we
440 sum over all pixels (which is what the likelihood measures), we can also examine the residuals as a function of position. We do
441 so in E.D. [Figure 6](#), which shows the measured *Fermi* counts in our ROI (summed in three energy bins) in the first column, our

best-fitting baseline + Sgr dSph model in the second column, and fractional residuals [(Data – Model)/Model] in the third column. The images are smoothed with a 0.5° Gaussian kernel, since this is roughly resolution of our interstellar gas maps [16, 18]. The plot shows that, on a point-by-point basis, our models reproduce the data within $\sim 10\%$, and that over most of the ROI the errors show no obvious spatial correlation. The only exception to this statement is a small ridge of correlated residuals at the South-West edge of the ROI, which are only at the $\sim 30\%$ level, and are far from the Sgr dSph region. This points to the existence of real structure in the Fermi Bubbles that is not yet perfectly modelled, but given the small level of the residuals and the distance between them and the signal in which we are interested, this modelling imperfection has little impact on our results.

As our second validation test, we evaluate the sensitivity of our pipeline to uncertainties in our templates for Galactic diffusion, and we verify that our pipeline can recover synthetic signals similar to the Sgr dSph even when our templates are imperfect. Recall that we have three components of Galactic diffuse emission for which the templates are at least somewhat uncertain: hadronic + bremsstrahlung emission (for which our template can be HD, Interpolated, or GALPROP), Galactic IC emission (for which the template can be 3D, 2D A, 2D B, or 2D C), and the Fermi Bubbles (for which the template can be S, structured, or U, unstructured). We test the sensitivity of our fits to these template choices as follows. First, we generate a set of mock background data by drawing a random realisation of photon counts from one combination of these templates, and on top of this we add a synthetic Sgr dSph signal; the Sgr dSph photons follow the spatial morphology of our Sgr dSph model I template, have a spectral shape $dN_\gamma/dE_\gamma \propto E_\gamma^{-2}$, and have a normalisation that we vary systematically from $\approx 10^{-11} \text{ ph cm}^{-2} \text{ s}^{-1}$ (integrated over all energies) to $\approx 10^{-5} \text{ ph cm}^{-2} \text{ s}^{-1}$; our best-fit Sgr dSph photon flux falls in the middle of this range, $\approx 2 \times 10^{-8} \text{ ph cm}^{-2} \text{ s}^{-1}$. Then we use our pipeline to recover the flux of the Sgr dSph from the synthetic map, but using a *different* set of templates for Galactic diffuse emission to the ones used to generate the synthetic data. Comparing the recovered Sgr dSph spectrum to the injected one reveals how well our pipeline performs when the input diffuse emission templates are not exactly correct. We carry out this experiment with four diffuse emission template combinations: (1) synthetic data generated from GALPROP + 3D + S, analysed using HD + 3D + S; (2) synthetic data generated from HD + 2D A + S, analysed using HD + 3D + S; (3) synthetic data generated from HD + 3D + S, analysed using HD + 3D + U; (4) synthetic data generated using HD + 3D + S, analysed using HD + 3D but no template for the FBs at all.

We show the results for the first two of these experiments in the two left panels of E. D. [Figure 7](#); the top left panel shows the recovered energy-integrated photon flux compared to the injected flux, while the bottom left shows the recovered spectra when the input flux is $\approx 2 \times 10^{-8} \text{ ph cm}^{-2} \text{ s}^{-1}$. The plot shows that our pipeline yields excellent agreement between the injected and recovered signals for both the integrated flux and the spectrum unless the Sgr dSph signal is ~ 1 order of magnitude weaker than our estimate. In no circumstance does our pipeline produce a false signal comparable in magnitude to our observed one. The two right panels of E. D. [Figure 7](#) show the third and fourth tests, where we mismatch the FB template. Here the effects are somewhat larger, but still relatively minor: if we create synthetic data with the S Fermi Bubble template (so that there is structure corresponding to the cocoon), and then analyse it using either the U template or no FB template at all, then we make a factor of $\sim 2 - 3$ level error in the absolute flux, but no substantial error in the spectral shape. This test suggests that our

475 detection of the Sgr dSph is very robust, but that we have a factor of $\sim 2 - 3$ uncertainty in its absolute flux, stemming from our
 476 imperfect knowledge of the foreground FBs.

477 Our third validation test is to check whether our fit degrades if we artificially rotate or translate the Sgr dSph template;
 478 if the signal we are detecting really does come from the Sgr dSph, the best fit should be for a template that traces its actual
 479 orientation and position, while rotated or shifted templates should produce progressively worse fits. To check if this is the case,
 480 we first rerun our analysis pipeline for our default set of templates (first line in [Table 1](#)), but with the Sgr dSph template rotated
 481 about its core. For each rotation angle we compute the TS, and compare to the TS of the original, unrotated model. We plot the
 482 result of this experiment in the left panel of E.D. [Figure 8](#). It is clear that, as expected, the fit is best when we use the actual
 483 orientation of the Sgr dSph, and degrades as we increase the rotation. Next, we carry out a similar procedure, but this time
 484 rather than rotating the Sgr dSph template about its core, we rotate around the centre of the Galaxy, thereby both translating and
 485 rotating the template. (This latter test was motivated by the particular alignment of the Sgr Stream with the previously claimed
 486 collimated jets from the Galaxy’s supermassive black hole [\[4\]](#).) We show the results in the middle panel of E.D. [Figure 8](#), and,
 487 again as expected, the TS strongly favours the true location and orientation of the Sgr dSph. Finally, we translate the Sgr dSph
 488 while leaving its orientation unchanged. We show the TS for displaced Sgr dSph in the right panel of E.D. [Figure 8](#). In this case
 489 find that the fit improves if we do displace the Sgr dSph from its true position by $\approx 4^\circ$ south. The amount by which the shift is
 490 favoured is fairly significant – the TS improved by 40.8, which corresponds to 4.5σ significance. Interestingly, the direction of
 491 the displacement is within a few degrees of the direction anti-parallel to the Sgr dSph’s proper motion, suggesting that the
 492 dwarfs γ -ray signal trails it slightly on its orbit. If IC-emitting CR e^\pm are largely responsible for the observed Sgr dSph γ -ray
 493 signal as suggested by our spectral modelling, a systematic displacement of this signal southward by $\sim 4^\circ$ from the stars of
 494 Sgr dSph is quite reasonable as we have explained elsewhere (and see [section 4](#)).

495 4 Transport of IC-emitting CR e^\pm

We have seen that, while our pipeline detects a signal from the Sgr dSph at very high statistical significance, the fit improves even more (by $\approx 4.5\sigma$) if we displace the Sgr dSph template $\approx 4^\circ$ from its actual position (corresponding to 1.9 kpc at the distance of the Sgr dSph), in a direction very close to anti-parallel to the dwarf’s proper motion. Here we demonstrate that a displacement of this type is expected in a model where the γ -ray signal from the Sgr dSph is powered by MSPs. Part of the MSP signal emerges directly from the MSP magnetospheres, and thus traces stellar component of the Sgr dSph. However, the majority of the observed signal is, in our model, IC emission powered by e^\pm escaping MSP magnetospheres and interacting with the CMB. The time between when e^\pm leave MSPs and when they IC scatter to produce γ -ray photons is non-negligible: the CMB is dominated by photons with energies $\sim k_B T_{\text{CMB}}$ (with $T_{\text{CMB}} = 2.7$ K), so IC photons with energies of $\sim 1 - 100$ GeV must be produced by e^\pm with energies $E_{e^\pm} \sim 0.6 - 6$ TeV. The characteristic IC loss time for such particles is

$$t_{\text{IC}} = \frac{3m_e^2 c^3}{4\sigma_T E_{e^\pm} U_{\text{CMB}}} = 1.2 \left(\frac{E_{e^\pm}}{\text{TeV}} \right)^{-1} \text{Myr}, \quad (11)$$

496 where m_e is the electron mass, c is the speed of light, σ_T is the Thomson cross section, and $U_{\text{CMB}} = a_R T_{\text{CMB}}^4 = 0.25 \text{ eV cm}^{-3}$
 497 is the energy density of the CMB.

During this time, the e^\pm will have the opportunity to move a significant distance prior to producing γ -rays, due to both bulk gas motion and CR flow relative to the gas. With regard to bulk advection, we note that the proper speed of the Sgr dSph is $\approx 260 \text{ km s}^{-1}$, and we therefore expect an effective wind of Galactic halo gas to be blowing through (or, at least, around) the dwarf at approximately this speed. This wind would advect the IC-radiating e^\pm southward. Quantitatively, the extent of the angular displacement of an IC γ -ray signal at E_γ

$$\Delta\theta_{\text{adv}}(E_\gamma) \simeq 1.0^\circ \left(\frac{E_\gamma}{\text{GeV}} \right)^{-1} \left(\frac{\nu_{\text{prop}}}{260 \text{ km/s}} \right) \quad (12)$$

498 where ν_{prop} is the proper motion on the sky. Thus advection is expected to generate a southward displacement of $\sim 1^\circ$.

This is less than the displacement we observe, but advection is also likely less important than CR transport through the gas. While the diffusion coefficient for CRs in the galactic halo is very poorly known, we can make an order of magnitude estimate by adopting the functional form for the diffusion coefficient given in ref [47] which is normalised to $3 \times 10^{27} \text{ cm}^2 \text{ s}^{-1}$ for a 1 GeV CR in a $3 \mu\text{G}$ field. Then the expected diffusive displacement of the IC-radiating e^\pm is

$$\Delta\theta_{\text{diff}}(E_\gamma) \simeq 3.5^\circ \left(\frac{E_\gamma}{\text{GeV}} \right)^{-0.12} \left(\frac{B}{0.1 \mu\text{G}} \right)^{-0.27}. \quad (13)$$

499 While this is roughly the correct amount of displacement to reproduce what we observe, if the diffusion were isotropic then we
 500 would still not have explained the systematic offset between the dwarf and the displaced location picked out by our template
 501 analysis. However, we do not expect isotropic diffusion in the environment of the Sgr dSph. Simulations of objects plunging
 502 through diffuse halo gas indicate that a generic outcome of such interactions is the development of a coherent magneto-tail
 503 back along the objects' direction of motion [48]. Such a structure formed by the Sgr dSph plunging through the Milky Way's
 504 halo would naturally explain why, rather than being isotropic, the diffusive transport is primarily backwards along the dwarf's
 505 trajectory.

506 **Supplementary Information References**

- 507 44. Yang, R.-Z., Aharonian, F. & Crocker, R. The Fermi bubbles revisited. *Astronomy & Astrophysics* **567**, A19. ISSN: 1432-
508 0746. doi:[10.1051/0004-6361/201423562](https://doi.org/10.1051/0004-6361/201423562). <http://dx.doi.org/10.1051/0004-6361/201423562>
509 (2014).
- 510 45. de Boer, W., Gebauer, I., Kunz, S. & Neumann, A. Evidence for a hadronic origin of the Fermi Bubbles and the Galactic
511 Excess. *arXiv e-prints*, arXiv:1509.05310 (2015).
- 512 46. Buschmann, M. et al. Foreground mismodeling and the point source explanation of the Fermi Galactic Center excess.
513 *Phys. Rev. D* **102**, 023023. doi:[10.1103/PhysRevD.102.023023](https://doi.org/10.1103/PhysRevD.102.023023) (2020).
- 514 47. Gabici, S., Aharonian, F. A. & Blasi, P. Gamma rays from molecular clouds. *Ap&SS* **309**, 365–371. doi:[10.1007/s10509-007-9427-6](https://doi.org/10.1007/s10509-007-9427-6) (2007).
- 515 48. Dursi, L. J. & Pfrommer, C. Draping of Cluster Magnetic Fields over Bullets and Bubbles—Morphology and Dynamic
516 Effects. *Astrophys. J.* **677**, 993–1018. doi:[10.1086/529371](https://doi.org/10.1086/529371) (2008).